

# Emission-Line Galaxies from the Hubble Space Telescope Probing Evolution and Reionization Spectroscopically (PEARS) Grism Survey. II: The Complete Sample

Nor Pirzkal<sup>1</sup>, Barry Rothberg<sup>1,2,3</sup>

Chun Ly<sup>1,4</sup>, Sangeeta Malhotra<sup>5</sup>, James E. Rhoads<sup>5</sup>, Norman A. Grogin<sup>1</sup>, Tomas Dahlen<sup>1</sup>,  
Gerhardt R. Meurer<sup>6</sup>, Jeremy R. Walsh<sup>7</sup>, Nimish P. Hathi<sup>8</sup>, Seth H. Cohen<sup>5</sup>, Andrea  
Bellini<sup>1</sup>, Benne W. Holwerda<sup>9</sup>, Amber N. Straughn<sup>10</sup>, Matthew Mechtley<sup>5</sup>

## ABSTRACT

We present a full analysis of the Probing Evolution And Reionization Spectroscopically (PEARS) slitless grism spectroscopic data obtained with the Advanced Camera for Surveys on *HST*. PEARS covers fields within both the Great Observatories Origins Deep Survey (GOODS) North and South fields, making it ideal as a random survey of galaxies, as well as the availability of a wide variety of ancillary observations to support the spectroscopic results. Using the PEARS data we are able to identify star forming galaxies within the redshift volume  $0 < z < 1.5$ . Star forming regions in the PEARS survey are pinpointed independently of the host galaxy. This method allows us to detect the presence of multiple emission line regions (ELRs) within a single galaxy. 1162 H $\alpha$ , [OIII] and/or [OII] emission lines have been identified in the PEARS sample of  $\sim 906$  galaxies down

---

<sup>1</sup>Space Telescope Science Institute, 3700 San Martin Drive, Baltimore, MD, 21210, USA

<sup>2</sup>George Mason University, Department of Physics & Astronomy, MS 3F3, 4400 University Drive, Fairfax, VA 22030, USA

<sup>3</sup>Leibniz-Institut für Astrophysik Potsdam (AIP), An der Sternwarte 16, 14482, Potsdam, Germany

<sup>4</sup>Giacconi Fellow

<sup>5</sup>School of Earth And Space Exploration, Arizona State University, Tempe, AZ, 85287-1404, USA

<sup>6</sup>International Centre for Radio Astronomy Research, The University of Western Australia, 35 Stirling Highway, Crawley, WA 6009, Australia

<sup>7</sup>European Southern Observatory, Karl-Schwarzschild-Strasse 2, D-85748 Garching, Germany

<sup>8</sup>Carnegie Observatories, 813 Santa Barbara Street, Pasadena, CA 91101, USA

<sup>9</sup>ESA Fellow, ESA-ESTEC, Keplerlaan 1, 2200 AG, Noordwijk, the Netherlands

<sup>10</sup>Astrophysics Science Division, Goddard Space Flight Center, Code 665, Greenbelt, MD 20771, USA

to a limiting flux of  $\sim 10^{-18}$  erg/s/cm<sup>2</sup>. The ELRs have also been compared to the properties of the host galaxy, including morphology, luminosity, and mass. From this analysis we find three key results: 1) The computed line luminosities show evidence of a flattening in the luminosity function with increasing redshift; 2) The star forming systems show evidence of disturbed morphologies, with star formation occurring predominantly within one effective (half-light) radius. However, the morphologies show no correlation with host stellar mass; and 3) The number density of star forming galaxies with  $M_* \geq 10^9 M_\odot$  decreases by an order of magnitude at  $z \leq 0.5$  relative to the number at  $0.5 < z < 0.9$  in support of the argument for galaxy downsizing.

*Subject headings:* line: identification, catalogs, galaxies: evolution, galaxies: luminosity function, mass function

## 1. Introduction

Emission line galaxies (ELGs) are systems selected by the presence of strong line emissions (e.g. Ly- $\alpha$ , [OII], [OIII], H $\beta$ , and H $\alpha$ ), usually detected using narrow band or grism surveys. The strong emission lines in these galaxies trace recent star formation activity, in contrast to the star formation history and properties of the global stellar populations that can be discerned using broad band observations. A significant amount of the light originating from ELGs is contained in regions producing strong emission lines which in turns makes these objects easily identifiable. The emission lines of ELGs also provide a convenient way to determine the redshift of these objects. Since ELGs are selected on the basis of strong emission lines rather than continuum emission, selecting ELGs allows one to probe down to lower luminosity (and thus lower mass) galaxies compared to broad band surveys which tend to be incomplete at or above  $m^*$  galaxies at more distant epochs. Assuming that ELGs are spatially distributed in a fashion similar to other galaxies, they provide a powerful tool for tracing the star formation history of the Universe.

The epoch  $0 < z < 1.5$  discussed in this paper is important because star formation activity in galaxies has been observed to increase significantly as redshift increases (e.g. Madau et al. 1998; Hopkins 2004). While at higher redshifts ( $z > 2$ ) there is still some controversy as to whether the star formation density relation flattens or decreases, the initial increase in star formation implies that, at low  $z$ , some mechanism(s) must have occurred which quickly quenched star formation. If this was not the case, massive ellipticals today would still be observed to be forming many stars. There is also evidence that suggest that the inter stellar

medium, star formation rates and gas fractions differ between local and distant galaxies. Studying galaxy evolution at these redshifts therefore does not only require the ability to measure the star formation history of these objects, but also depends on our ability to properly sample galaxies over a wide range of masses to alleviate as many biases as possible. ELGs are ideal for such work. As noted above, these objects are easily detected in surveys and they are efficient for probing to lower stellar masses as a function of telescope time required. The wavelength range of the ACS grism used for PEARS makes it possible to identify the strong rest-frame emission lines that are well known to be a sign of vigorous star formation (e.g.  $H\alpha$ , [OIII] and [OII]) out to  $z \sim 1.5$ . In fact, in this paper, examining  $H\alpha$ , [OIII] and [OII] emitters separately allows us to look at properties of star forming galaxies in increasing redshift ranges. When plotted separately, these three emission lines represent proxies for the redshift bins of  $0 < z < 0.5$ ,  $0.1 < z < 0.9$ , and  $0.5 < z < 1.5$ , respectively.

Identifying ELGs has traditionally been done using narrow band photometric filters. This technique has even been successfully applied to very high redshifts to detect Ly- $\alpha$  emitters (Rhoads et al. 2001). However, while narrow band surveys can efficiently cover large fields of view down to relatively faint magnitudes, they are typically limited to very small and discrete redshift ranges. This can be partially alleviated using multiple narrow band filters (e.g. Subaru Deep Field, Ly et al. 2007) but continuous redshift coverage remains intrinsically limited in narrow band surveys. The Probing Evolution And Reionization Spectroscopically (PEARS) slitless grism spectroscopic survey provides an unprecedented opportunity to study ELGs in a way that cannot be achieved from any ground based observations. PEARS allows us to bypass the difficulties inherent in narrow band filter surveys (as noted above) and the limitations imposed by varying sky brightness and atmospheric emission lines which can limit ground-based grism surveys, and identify ELGs based *solely* on the direct detection of emission lines in dispersed slitless spectra. As previously shown (Pirzkal et al. 2006; Straughn et al. 2008, 2009), this approach allows us to detect emission lines in very faint host galaxies, particularly sub- $m^*$  galaxies, over a very large and continuous redshift range and is particularly sensitive to high EW emission lines. Particular to the PEARS survey, the use multiple position angles on the sky allows us to identify emission lines using independent observations as well as to pinpoint the exact physical location of the ELRs within each ELG. Crucially, and in addition to this, the PEARS survey was designed to overlap with both the GOODS-N and GOODS-S fields, and there is therefore a substantial amount of ancillary data available, including very deep, high resolution broad band imaging ranging from the UV to the infrared bands.

As we noted above, the redshift range ( $0 < z < 1.5$ ) probed by PEARS is a critical transition epoch, both in terms of star formation histories and morphological evolution. On one

hand, the PEARS grism slitless observations make it possible to efficiently identify emission lines, identify the corresponding ELRs and host ELGs. On the other hand, the GOODS ancillary data allow us to examine the morphology and physical characteristics of the ELGs. This powerful combination of data gives us an opportunity to examine the evolution of ELGs over a long period of time and over a much wider mass range than has been previously probed.

This paper is organized as follow: Section 2 briefly summarizes the PEARS observations (HST Proposal 10530, P.I. Malhotra). Section 3 describes the data reduction and analysis of the sample, including detection, extraction and identification of emission lines, as well as completeness tests. Section 4.1 presents the PEARS [OII], [OIII] and  $H\alpha$  line luminosity functions and their redshift evolution. Finally, Section 4.2 compares the properties of the PEARS host galaxies, such as morphology and luminosity, with the star formation properties discerned from the PEARS emission lines. All calculations in this paper assume  $H_0 = 70 \text{ km s}^{-1} \text{ Mpc}^{-1}$  and  $\Omega_M = 0.3$ ,  $\Omega_\Lambda = 0.7$ . All magnitudes are given in the AB system.

## 2. Observations

The PEARS observations were obtained as part of a large *Hubble Space Telescope* (HST) proposal (200 orbits, Proposal 10530; P.I.: Malhotra). The program used the Advanced Camera for Surveys (ACS) Wide Field Camera (WFC) in conjunction with the G800L grism filter. The G800L has a resolution of  $R \sim 69\text{-}131$  and provides wavelength coverage of  $0.55\text{-}1.05 \mu\text{m}$  across the entire ACS/WFC field of view. A total of nine fields ( $\approx 11.65 \text{ arcmin}^2$  for each field) were observed for  $\approx 40000 \text{ s}$  (20 orbits) each, split evenly between observations taken at different position angles (P.A.) on the sky (typically 3 per pointing). Multiple P.A.s are important for identifying and masking contamination from other sources in the field and removing spurious pixels (e.g. cosmic rays, bad pixels, etc). Four PEARS fields are within the GOODS-N field (Giavalisco et al. 2004). Five PEARS fields are within the GOODS-S field, with one PEARS field re-observing the GRAPES/HUDF field (Pirzkal et al. 2004). The combined areas of the PEARS-N and PEARS-S are  $50.24$  and  $68.84 \text{ arcmin}^2$ , respectively. The fields and their location within the GOODS fields are shown in Figure 1. Table 1 lists the PEARS fields positions and total exposure times.

### 3. Data Reduction and Analysis

#### 3.1. Detection of Emission Lines

PEARS emission lines were initially detected directly from combined high signal to noise ACS grism slitless spectroscopic images. The method does not rely on and is independent of any imaging data or object catalog. The basic method used to identify emission lines in the PEARs data was described in Straughn et al. (2008, 2009). However, at that time, only the PEARs-S data were used. We now present the full PEARs dataset (comprising of PEARs-N and PEARs-S) which covers an area on the sky that is approximately twice as large. We have also employed a new, slightly refined version of our line identification pipeline and are able to reach down to a slightly lower flux level than before. The detection algorithm, dubbed “PEARs-2D,” is very briefly summarized below and was applied to each of the individual 9 PEARs fields listed in Table 1:

- 1) All grism exposures obtained at the same P.A. on the sky are combined using the PYRAF task MULTIDRIZZLE (Koekemoer 2002). This produces a high signal to noise image that is free of cosmic-ray and detector artifacts. This image is then smoothed using a  $13 \times 3$  median to produce a smooth high signal-to-noise grism image of the field.
- 2) The smoothed image is subtracted from the combined Multidrizzle image of the field. This step essentially removes the underlying continuum emission from the dispersed spectra. The resulting continuum subtracted image is what we use to detect emission lines.
- 3) Using SExtractor (Bertin & Arnouts 1996) and the continuum subtracted image, we identify point sources, e.g. emission lines, noise spikes, and detector artifacts. This step generates a list of emission line candidates for each P.A.
- 4) Steps 1 through 3 are repeated separately for each available P.A. resulting in 3 or 4 (i.e. the number of available P.A.s) emission line candidates lists.
- 5) Using a detailed knowledge of the instrument distortions and of the dispersion relation of the G800L ACS/WFC grism, and combining the data obtained using multiple P.A.s, we determine the location on the sky where each individual emission line originates (essentially where the different traces cross when projected onto the sky) as well as determine the observed wavelength of each emission line. We derive a unique wavelength for each line in each of the available P.A. (See Figure 2 of Straughn et al. 2008).

The PEARs-2D method was applied separately to each PEARs field listed in Table 1 and a separate list of ELR candidates was therefore generated for each of the nine PEARs fields, ignoring for now the fact that some of these fields overlap slightly. The number of ELR candidates that was generated was controlled mainly by the detection threshold used to detect emission lines with SExtractor and by how much tolerance we allowed in the inferred

ELR positions and observed wavelengths of the emission lines. We adopted a detection of  $1.1\sigma$  per P.A., which for a line detected independently using 3 different P.A.s corresponds approximately to a  $2\sigma$  detection. We also allowed for a 3 pixels tolerance in the physical location of an ELR (accounting for an imperfect knowledge of the trace of the ACS grism) and a  $100\text{\AA}$  tolerance in the wavelength we derive for an emission line (again accounting for an imperfect knowledge of the wavelength solution of the ACS grism). While the use of multiple P.A.s was quite effective at filtering spurious detections, our tolerance limits and aggressive detection threshold resulted in the detection of fainter emission lines, at the cost of some false positive detections.

Using the PEARS-2D method allowed us to generate a list of ELR candidates for each PEARS field that did not rely at all on any pre-generated object catalogs or pre-selection of target galaxies. We stress that a candidate ELR did *not* require the detection of a host galaxy in the field. PEARS-2D, with its multiple P.A.s strategy, has three immediate advantages over other methods that rely on observations taken at a single P.A.: First, we can expect to detect extremely large EWs that would not be identified through more traditional techniques. Second, we derive accurate locations of ELRs without assuming that the source is at the center of the host galaxy and we can therefore identify multiple ELRs within a single galaxy. Finally, the PEARS-2D line wavelength calibration is significantly more accurate. Normally, the wavelength reference point is tied to the location of the host galaxy (determined using a direct image taken in conjunction with the grism observations). However, since ELRs can be several half-light radii away (amounting to a non-trivial number of pixels) the wavelength solution of the ELR is affected by this distance from the center of the host galaxy. Every error of one pixel in the assumed position of the emission line feature results in a  $40\text{\AA}$  systematic error in wavelength calibration. For large galaxies with multiple ELRs this can lead to errors on the order of several hundred  $\text{\AA}$ . Using the PEARS-2D, this error is avoided because the wavelength solution of the ELRs is determined *independent* of any information about the host galaxy.

### 3.2. Extraction and Verification of Spectra

We extracted spectra of the ELRs candidates identified in Section 3.1 using the PEARS grism data reduction pipeline (e.g. Pirzkal et al. 2009). However, our pipeline was modified so that we used the positions of the ELRs candidates (i.e. the source of the emission features detected in our grism exposures) rather than a catalog of objects derived from the GOODS broad-band images. The extraction and calibration of the spectra were performed with

aXe (Pirzkal et al. 2001; Kümmel et al. 2009) using optimally weighted extractions and an extraction width of  $3\times$  the measured emission regions sizes. Individual spectra were extracted from single ACS grism exposures and spectra taken at the same P.A. were then combined using aXeDrizzle. We thus obtained between 3 to 4 independent spectra for each of our ELR candidate (one per available P.A.). Wavelength and flux calibration were performed by aXe using the STScI provided calibration files for the ACS G800L grism. Emission lines fluxes were measured using gaussian fitting in each extracted spectra, resulting in 3 to 4 measurements. We then computed the average line flux and associated standard deviation value for each of our emission line candidates. These line fluxes were corrected for Galactic Reddening assuming values from Cardelli et al. (1989). The corrections were negligible with  $E(B-V)=0.012$  for PEARS-N fields and  $E(B-V)=0.0078$  for PEARS-S fields.

Our list of ELR candidates reached down to very low flux levels and contained many false positives, we therefore had to vet each ELR and its associated emission line candidates. While we attempted to apply automatic techniques to accept or reject ELR and emission line candidates, we found it useful to manually vet spectra by eye. Authors of this paper manually examined and graded emission lines on a scale ranging from 0 (very poor) to 5 (very high). Each emission lines were graded a minimum of 3 times and by at least two different persons and the average of this grade was adopted. A final grade of 2 was found to correspond to a marginal  $\approx 2$  sigma detection of spectra obtained in at least two separate P.A.s.

We originally identified a total of 3705 emission line candidates using the PEARS-2D method described in Section 3.1. The visual quality assessment yielded a sample of 1162 marginally detected emission lines (529 in PEARS-N and 633 in PEARS-S). As multiple emission lines were sometimes detected in an ELR, the final number of ELRs was 985 (451 in PEARS-N and 535 in PEARS-S).

### 3.3. Emission Line & Host Galaxy Identification

Determining the nature of emission lines in the extracted spectra of a given ELR fell into two distinct categories: either multiple emission lines were detected or only a single emission line was detected.

The resolution of the G800L grism is  $40\text{\AA pixel}^{-1}$  and is too low to resolve and identify close emission line pairs (e.g. [OIII] and  $H\beta$ ). However, in the redshift range of the PEARS survey ( $0 < z < 1.5$ ), there are pairs of widely separated emission lines that allow for both line identification (via the ratio of the observed wavelengths of the two lines) and redshifts to be determined. The line pairs that we considered were: [OII] and [OIII]; [OIII] and  $H\alpha$ ; or CIII] and CIV.

However, most of the time spectra contained only one prominent emission line and we had to rely on a comparisons with photometric redshifts of the host galaxy from Dahlen et al. (2010, 2012). While we noted above that the PEARS ELRs were selected independently, we subsequently matched them with a host galaxy in the GOODS fields. We used the public ACS GOODS 2.0 data to generate mosaics of the GOODS fields and used SExtractor to generate segmentation maps and object catalogs of galaxies for these fields. In the great majority of cases, the RA and DEC of a PEARS ELR clearly fell within the segmentation map of a galaxy. In such cases the corresponding galaxy was assumed to be the host of the ELR and we assumed the redshift of the observed emission lines to be the known photometric redshift for the host galaxy. Some ELRs ( $\approx 6\%$  of objects with a significant emission line with a grade of 2.5 or larger) were found to lie beyond any galaxy segmentation maps. In such cases, we adopted the photometric redshift of the GOODS object with the closest segmentation map (which not necessarily the closest object in cases of large extended galaxies). When comparing photometric redshifts to PEARS spectroscopic redshifts obtained using one of the pair of emission lines listed above, we found that in 94% of the case the redshifts we derive are within the 95% confidence regions given for the photometric redshifts of Dahlen et al. (2010, 2012).

When only a single emission line was detected in a spectrum, we assumed that it could be either Ly- $\alpha$ , CIV, CIII], MgII, [OII], [NeIII], [OIII], H $\gamma$ , or H $\alpha$ , observed at the assumed GOODS photometric redshift value. We identified the type of the emission line and computed a spectroscopic redshift for that object simply by selecting the line type that produced the closest match to the observed wavelength.

We acknowledge that some of the emission lines discussed in this paper are blended lines, but this should have little effect on our analysis as weaker lines only weakly bias the fluxes and redshifts we derive. This is the case for example for [OIII] which is really two unresolved lines at 4959Å and 5007Å, H $\alpha$  at 6562Å which is blended with weaker [NII] at 6583Å, while by [NeIII] we actually refers to the stronger component at 3868Å).

Some for the PEARS ELGs were found to contain more than one ELRs. Since these ELRs and the emission lines their spectra contained were analyzed separately, this provides us with a way to check the consistency of the PEARS spectroscopic redshifts. We found that in these cases the redshifts agreed to within  $z = \pm 0.01$ , demonstrating excellent consistency. We briefly noted above that some of the PEARS fields overlap slightly. Some ELRs were therefore observed and analyzed independently as part of different PEARS fields. We found that 19 ELRs were observed twice (15 in PEARS-N and 4 in PEARS-S. The higher number of duplicate observations in PEARS-N is the result of the larger amount of overlapping between individual PEARS-N fields, as shown in Figure 1). Comparing the observed emission lines wavelength, the emission line fluxes and finally the redshifts, we find that our errors were:



$\langle \delta\lambda \rangle = 18\text{\AA}$ ;  $\langle \frac{\delta f}{f} \rangle = 8\%$ ; and  $\langle \delta z \rangle = 0.003$ , again demonstrating excellent consistency.

For the remainder of this paper, noting that emission lines with a grade of 2 constitute a marginal detection, we adopt a minimum emission line grade of 2.5 or greater (corresponding to a line flux limit of approximately  $5 \times 10^{-18}$  erg/s/cm<sup>2</sup>) when deriving properties of H $\alpha$ , [OIII] and [OII] emitters (174, 401, and 167 lines, respectively).

### 3.4. Spectroscopic vs. Photometric Equivalent Widths for ELRs at Large Radii

One of the advantages of PEARS-2D is the ability to detect multiple ELRs within a single galaxy (see Figure 2). However, at progressively larger radii from the galaxy center the contribution from the underlying continuum decreases. Since spectra are extracted at these large radii using small extraction windows, the measured EWs are generally larger than what would be derived by simply comparing the measured line fluxes to the total underlying continuum of the host galaxy. The EWs derived from narrow band imaging surveys generally rely on the latter method. To quantify any potential differences photometric EWs (EW<sub>phot</sub>) were computed using the measured PEARS line flux and the measured total host galaxy broad band flux. On average the spectroscopic EW (EW<sub>spec</sub>) was  $\sim 3.5 \times$  (EW<sub>phot</sub>). Histograms of the EW<sub>spec</sub>s for the H $\alpha$ , [OIII], and [OII] are plotted in Figure 3. We note that for the purposes of this paper an emission line is reported as a positive EW.

### 3.5. Blended Emission [OIII] and H $\beta$ Lines

The ACS G800L grism cannot separate the [OIII] doublet (4959 $\text{\AA}$ , 5007 $\text{\AA}$ ) and H $\beta$  (4681 $\text{\AA}$ ). These three lines appear blended in the PEARS spectra and H $\beta$  can appear as an asymmetric feature to the stronger [OIII] line. To correct the [OIII] fluxes, each of the lines were fit using separate components. We assumed identical full width at half maximum and assumed a fixed wavelength separation for all three lines. Based on this we obtained estimates of the [OIII] to H $\beta$  lines ratio for the ELRs. We found  $\frac{f(H\beta)}{f([OIII])} \approx 0.23 \pm 0.25$ , which is consistent with the relative fluxes expected in star forming galaxies (Juneau et al. 2011).

### 3.6. Comparison with Previous PEARS-S Catalog

The PEARS-S data were analyzed and published by Straughn et al. (2009) and are included as part of our analysis of the complete PEARS survey. While our improved analysis reaches down to fainter observed flux levels, which directly results in a larger number of ELRs being detected, our emission line list contains in excess of 90% of the emission lines listed in Straughn et al. (2009). However, the number of  $H\alpha$ , [OIII], and [OII] emission lines (with a grade of 2.5 or above) are 1.2, 1.6, and 2.7 times higher than in the Straughn et al. (2009) catalog, respectively. This is a direct result of our ability to reliably detect fainter emission lines in these data, which particularly affects the intrinsically fainter [OIII] and [OII] emission lines. Our use of optimal weighted extraction, as opposed to narrow box extraction (increasing signal-to-noise at the expense of flux completeness) as was the case in Straughn et al. (2009), results in more reliable flux measurements of these emission lines and the lines fluxes we measure are on average twice of those listed in Straughn et al. (2009).

### 3.7. Completeness Simulations

Table 4 lists the median and average line fluxes for  $H\alpha$ , [OIII], and [OII] with a strong detection (PEARS grade of at least 2.5). In Figure 4 we show the distributions of the line fluxes for these three lines. The histograms are plotted as a fraction of the total for each line. Figure 4 demonstrates that the PEARS-2D line fluxes peak at values of  $\sim 10^{-17}$  erg/s/cm<sup>2</sup>. The ACS G800L grism has an approximately flat sensitivity from  $\approx 6000\text{\AA}$  to  $9500\text{\AA}$ , but our ability to recover emission lines from the two dimensional dispersed images needs to be carefully evaluated before we can say anything about the volume density of these sources. We determined the PEARS-2D detection limits using extensive end-to-end monte carlo simulations. These steps are briefly outlined here: First, we started with the real individual PEARS ACS/WFC G800L exposures and artificially added a random distribution of simulated ELRs (and simulated emission lines) to these data. We allowed for a wide ranges of line fluxes, host galaxies, and redshifts in these simulations and also allowed for random placement of multiple ELRs in each galaxy. Each of the nine PEARS field was simulated ten times, each time adding ELRs to 100 galaxies.

Next, the simulated data were processed and identified using exactly the same procedures used for the real observations. The simulated spectra were then extracted using aXe and line fluxes measured as we described in Section 3.2. Comparing input and output line lists, we found that the PEARS wavelength sensitivity is very similar to the inverse sensitivity of the ACS G800L grism with sharp cutoff below  $5500\text{\AA}$  and above  $9500\text{\AA}$ . This set the redshift limits of the PEARS survey for the  $H\alpha$ , [OIII] and [OII] lines to be  $0 < z < 0.5$ ,

$0.1 < z < 0.9$ ,  $0.5 < z < 1.5$ , respectively. We also found PEARS was mainly limited by the intrinsic emission line flux, that ELRs with emission lines containing fluxes as low as  $10^{-18} \text{erg/s/cm}^2$  could be detected and that we could detect more than 50% of emission lines with flux greater than  $\approx 3 \times 10^{-17} \text{erg/s/cm}^2$ . We also determined that we could detect emission lines with  $\text{EW} > 50 \text{\AA}$ . This is consistent with the observations of observed line fluxes shown in Figure 4. The exact fractions of lines recovered as a function of observed line flux for the PEARS-N, PEARS-S and PEARS-S-HUDF field (which is twice as deep as the other PEARS-S fields) are shown in Figure 5. A emission line grade of 2.5 corresponds to a line flux of approximately  $5 \times 10^{-18} \text{ erg/s/cm}^2$ .

### 3.8. Methods for Computing Luminosity Functions and SED Fitting

We briefly describe the methods we adopted to determine the PEARS emission line luminosity functions for  $\text{H}\alpha$ , [OIII] and [OII]. We also outline how we derive stellar masses for the ELGs containing the ELRs we identified in the previous Sections. Finally, we discuss the different approaches we adopted to account for internal dust corrections when computing the PEARS line luminosity functions.

#### 3.8.1. The $1/V_{\text{max}}$ method

This widely used method does not assume a shape for the luminosity function  $\Phi(L)$ . However, one disadvantage is that it requires the data to be binned. The number of bins can impact the results. In this paper, the number of bins was determined using the Freedman-Diaconis rule (Freedman & Diaconis 1981), whereby the bin size is selected to be  $2 \text{ IQR}(x)n^{-\frac{1}{3}}$ , where IQR is the interquartile range of the data and  $n$  is the number of data points in the sample. Using the  $1/V_{\text{max}}$  method, the luminosity function is computed using the following formula:

$$\Phi(\log L_i) = \frac{1}{\Delta \log L} \sum_j \frac{1}{f(z_j, L_j) V_j} \quad (1)$$

where:  $|\log L - \log L_i| < \frac{1}{2} \Delta \log L$ ;  $\Delta \log L$  is the bin width;  $V_j$  is the maximum volume within which object  $j$  (observed to have a line flux of  $l_j$  and to be at the redshift of  $z_j$ ) would be detected in our survey; and  $f(z_j, L_j)$  is the incompleteness  $f(l)$  (see 3.7) remapped into absolute luminosity space  $L$  given the object's redshift  $z_j$ , and is defined as:

$$V_j = \frac{\Omega}{4\pi} \int_{z_{j,\min}}^{z_{j,\max}} \frac{R(z)dV_c(z)}{dz} dz \quad (2)$$

where:  $\Omega$  is the solid angle of our survey (sr);  $V_c(z)$  is the cosmological comoving volume at redshift  $z$  (in  $\text{Mpc}^3$ );  $R(z)$  is the normalized grism response function expressed as a function of object redshift; Given the redshift range  $\{z_l, z_h\}$  at which a given emission line can be observed by the ACS grism (i.e. observed at wavelengths  $6000\text{\AA} < \lambda < 9000\text{\AA}$ ), the minimum redshift,  $z_{j,\min}$  is  $z_l$  while the maximum redshift  $z_{j,\max} = \min(z_h, z_{\text{faint}})$ , where  $z_{\text{faint}}$  is the maximum redshift at which a line with luminosity  $L$  would remain above our minimum line detection threshold  $l_{\text{threshold}}$ . Hence,  $z_{\text{faint}}$  is the redshift corresponding to the distance of  $D_L(z_j)\sqrt{l_j/l_{\text{threshold}}}$ , where  $D_L(z_j)$  is the luminosity distance of object  $j$ .

### 3.8.2. STY method

The STY method is another commonly used method for estimating the luminosity function. In this one, one assumes that  $\Phi(L)$  has the form of a Schechter function (Schechter 1976):

$$\Phi(L)dL = \Phi_* \left(\frac{L}{L_*}\right)^\alpha \exp\left(-\frac{L}{L_*}\right) \frac{dL}{L_*} \quad (3)$$

which is characterized by the three parameters  $\alpha$ ,  $\Phi_*$ , and  $L_*$ . Following from Sandage et al. (1979), the probability of observing a given object  $j$  at redshift  $z$  with a luminosity  $L_j$ , is then:

$$p(L_j, z_j) = \frac{\Phi(L)f(z_j, L_j)R(z_j)}{\int_{L_{\text{faint}}}^{\infty} \Phi(L)f(z_j, L)dL} \quad (4)$$

The joint likelihood can then be computed for the whole group of observed lines:

$$L = \prod_j p(L_j, z_j) \quad (5)$$

From this, can then determine values of  $\alpha$  and  $L_*$  that maximizes this likelihood. The overall normalization constant  $\Phi_*$  cannot be determined this way, because it cancels out in Equation 4. In this paper, we determined the values of  $\alpha$  and  $L_*$  by maximizing Equation 5 using a Monte Carlo Markov Chain approach. This allowed us to determine the most likely values of these two parameters as well as 95% credible intervals for these parameters.  $\Phi_*$

was computed by integrating Equation 3 and normalizing the result so that matched the number of detected objects.  $\Phi_*$  was computed for each combination of  $\alpha$  and  $L_*$  in our Markov Chains to produce 95% credible intervals for the parameter  $\Phi_*$ .

### 3.8.3. Host galaxy SED fitting

Properties of the host galaxies of the PEARS ELRs were estimated by fitting model Spectral Energy Distributions (SEDs) to their broadband photometric colors. The photometric values were taken from the TFIT GOODS measurements, which include 10 and 12 photometric bands in the GOODS-N and GOODS-S, respectively (Laidler et al. 2007; Grogin et al. 2012). The photometry spans the observed UV (*U*-band) through thermal-IR based on VLT, *HST* and *Spitzer* observations. The actual SED fitting was done using our own Monte Carlo Markov Chain SED fitting code ( $\pi\text{MC}^2$ ) (Pirzkal et al. 2012) to obtain estimates of the stellar masses, extinction, and ages of the host galaxies.  $\pi\text{MC}^2$  is a far more robust method of SED fitting than the standard  $\chi^2$  algorithms because it takes into account a proper treatment of both error propagation and computation of confidence levels. A more detailed explanation of MCMC can be found in (Pirzkal et al. 2012) and references within.

A simple stellar population model from BC03 (Bruzual and Charlot 2003) templates and a Salpeter IMF were used. While the choice of IMF and input models (e.g. BC03 or Maraston (Maraston 2005)) can affect derived stellar masses, the effects are not the same at all redshifts. The detailed simulations presented in Pirzkal et al. (2012) show that for the redshift range of interest here, stellar mass estimates from different models are consistent with each other to within a factor of a few. Other parameters obtained from SED fitting (e.g. extinction, metallicity and ages of the stellar population) are significantly more uncertain. For the purposes of this paper, we are primarily concerned with stellar mass, and to some extent extinction. In Figure 6 we show the distribution of stellar masses and extinctions for the host galaxies of the PEARS emission line sample. The mean stellar masses of the host ELGs are  $\text{Log}(\text{mass}) = 8.74 \pm 0.97 \text{ M}_\odot$ . We also estimate that the continuum extinction is relatively low with an average value of  $A_V = 0.87 \pm 0.88 \text{ mag}$ .

### 3.8.4. Internal Dust corrections to Luminosity Functions

Using the current PEARS data, there was no way to directly infer the amount of internal (to the host galaxy) dust attenuation affecting the line luminosities. We tested three methods for approximating dust corrections and compared the dust correction luminosity

functions to the ones from Ly et al. (2007). The first dust correction used attenuation values from the individual SED fits to the host galaxies. The second method relied on applying an average extinction value of  $A_{H\alpha} = 1.0$  mag (corresponding to  $A_{[OII]} = 1.88$  mag and  $A_{[OIII]} = 1.36$  mag), as is commonly done in such a case (Hopkins 2004; Takahashi et al. 2007). The third method relied on a dust correction based on the somewhat more sophisticated luminosity dependent dust correction of Hopkins et al. (2001)

While the two first approaches are straight forward, they are a rather curve attempt at applying dust correction. Indeed, these approaches do not allow for the extinction values within ELRs to be different than the host galaxy as a whole and therefore do not allow for the possibility that ELRs might contain different amount of dust than the host galaxy as a whole. The luminosity dependent approach empirically attempts to circumvent this limitation. In this case, the amount of dust correction is correlated the the measured line luminosities. This method, unlike the first two, could in principle effect the shape of the luminosity functions that we measure.

We find however that the three methods of correcting for dust have only limited influence on the luminosity functions. Either simply shifting the luminosity functions by a fixed amount without affecting the slope ( $\alpha$ ) at all (as is the case when using the first two methods), or additionally only altering the slope ( $\alpha$ ) slightly (as is the case when applying a luminosity dependent dust correction). As expected, the [OII] lines were more affected by dust than the [OIII] and  $H\alpha$  lines. However, in totem, for  $H\alpha$ , [OIII] and [OII] the slopes varied by only  $\sim 0.1$  on average using either of the three methods discussed above, and we conclude that the effect of dust correction on the slope of the luminosity functions is therefore negligible.

## 4. Results

### 4.1. The Emission Line Regions

#### 4.1.1. Star Forming Galaxy Density

Using the uncorrected PEARS lines listed in Table 4, we can compute a space density of star forming galaxy (SFG), as measured by the PEARS survey, and compare it to previous ACS grism based surveys. We estimate the star forming galaxy density at  $0.3 < z < 1.3$  to be  $4.5 \times 10^{-3} \text{ Mpc}^{-3}$ . This is in complete agreement with previous pure parallel ACS grism surveys such as the one described in Drozdovsky et al. (2005).

#### 4.1.2. Luminosity Functions

We computed the luminosity functions for the  $H\alpha$ , [OIII], and [OII] samples using both the  $1/V_{\text{max}}$  method and the STY methods that we described in Sections 3.8.1 and 3.8.2. The non dust-corrected luminosity functions, computed using the  $1/V_{\text{max}}$  method are shown in Figures 7 to 9. In these figures, the new measurements are compared to those of (Ly et al. 2007, shown with open triangles and also uncorrected for dust). We added one additional constraint to the data from Ly et al. (2007). The comparisons were made only with objects from that paper with an EWs  $> 50\text{\AA}$ .

The results from PEARS agree fairly well with earlier results, although they probe lower line luminosities for [OIII] and  $H\alpha$ . The  $1/V_{\text{max}}$  results from PEARS-N and PEARS-S are plotted separately in Figures 7 to 9. The differences between these two large and independent fields are well within the errors. Table 5 summarizes the results from fitting the luminosity functions to each of the emission lines in each field separately and PEARS-N and -S together for both the  $1/V_{\text{max}}$  and STY methods. Table 5 also includes the associated 95% credible intervals.

When using the  $1/V_{\text{max}}$  method, as previously noted in Section 3.8.1, the choose of bin size is important. We illustrate the effect of various bin sizes by showing (using light shaded circles) the luminosity functions we compute while allowing the bin sizes to vary. As one can visually witness, the effect of bin size has an immediate effect on the values with derive at a given luminosity. We show the luminosity derived using the optimal bin sizes using solid symbols. Error bars associated with individual points were derived using a few thousands bootstrapping iterations.

Here, we briefly note that the STY method produces steeper slopes than  $1/V_{\text{max}}$  for [OII]. Yet for [OIII] and  $H\alpha$  the two methods are consistent with each other. The differences between the two are likely due to the limited number of sources over a wide redshift range. This underlines the difficulties in obtaining luminosity function estimates with limited numbers of sources as well as the impact of different methods for deriving those estimates. We further note that the results shown in Figures 7 to 9 are also generally consistent with those from Ly et al. (2007).

#### 4.1.3. Do Luminosity Functions Evolve with Redshift?

Two advantages of the PEARS-2D sample are: that it reaches to faint line fluxes (a few times  $10^{-18}\text{erg/s/cm}^2$ ); and its the wide redshift range coverage. These can be used to investigate whether or not the slope of the luminosity functions changes with redshift. A change in the slope of the luminosity function as a function of redshift is a strong indication

of evolution of how star formation has been occurring in the past  $\approx 9$  billions years. To examine this issue, each of the emission lines was divided by redshift, first into two bins, then into three bins. We used two different number of bins to provide for a consistency check of our results. A luminosity function was fit to the data in each redshift bin (see Table 5). This allowed us to compute slopes for different redshift ranges. These slopes are plotted against redshift in Figure 10. The “resolution” (number of bins) in Figure 10 is limited by the available number of sources. Figure 10 shows a significant decrease in the value of  $\alpha$  as redshift increases for  $H\alpha$ , [OIII], and [OII] at both “resolutions.” This is consistent with earlier results from Ly et al. (2007). It suggests an evolution in ELGs and their capability to form stars over the last several Gyr as the proportion of high to low SFR regions increases as redshift increases.

#### 4.1.4. *The Spatial Distribution of ELRs*

A major difference between PEARS-2D and other ELG studies is that we are able to detect the presence of multiple ELRs within a single galaxy. A breakdown of the sample shows that 69% of the ELGs contain a single ELR; 24% contain two ELRs; 4% contain three ELRs; and 3% contain four or five ELRs. Comparing the location of the ELR, as parametrized by their distance to the center of the host ELG normalized by the half-light radius of the host ELG, we can compare the distribution of single emission line regions to the distribution of multiple emission line regions. Figure 11 shows there is no indication of any strong differences between the two samples. In both cases, the emission line regions appear to be predominantly located around one half-light radius from the center of the ELG. We compute a Kolmogorov-Smirnov test (KS) p-value of 0.49 which indicates that these distributions are statistically identical.

#### 4.1.5. *Star Formation Rates of ELGs*

One of the most important question in galaxy evolution is whether the SFR changes over time, and if so, what shape does SFR vs redshift have. Assuming that ELGs are representative of star forming galaxies in general, the depth of the PEARS-2D study and the large redshift range allows us to tackle this important question. The SFR was calculated for the [OII] and  $H\alpha$  emission lines using the Kennicutt (1998) relations. For [OIII] which are likely to actually be blended [OIII] and  $H\beta$  the relation from Equation 5 in Drozdovsky et al. (2005) was adopted. The results are shown, as a function of redshift in Figure 12. Also plotted (using a black solid line) is the SFR for emission lines with an observed flux of



$3 \times 10^{-17} \text{erg/s/cm}^2$ . This corresponds to the PEARS-2D 80% completeness level (solid black solid line). This illustrates our ability to detect emission line uniformly from  $0 < z < 1.5$ .

Simply computing the SFR does not provide an entirely accurate assessment of star formation because the mass of the galaxy affects the rate at which stars form. Instead, one can normalize the SFR by the mass of the galaxy (in this case estimated from the stellar masses computed in Section 3.8.3) to derive the specific SFR (sSFR). A histogram of the sSFR for the PEARS-2D ELGs is shown in Figure 13.

As the sSFR value of a galaxy can be taken, as a rough approximation, as one over the built up time of a galaxy, assuming constant star formation rate, the PEARS ELGs sSFRs implies a possible stellar mass built-up time of a few billions years. Note however that these sSFR estimates should be considered to be lower limits since some non detected star formation might be present in the PEARS ELGs and the SFR values we quote are not corrected for extinction.

There has been some discussion (Guo et al. 2011) as to whether the SFR in star forming regions of galaxies should be correlated to the location of the star forming regions within the galaxy. We investigate this possible relation using the PEARS ELG sample. Figure 14 shows a plot of the estimated SFR of each ELR in the PEARS-2D sample, separating  $\text{H}\alpha$ , [OIII] and [OII] emitting regions, as a function of radial distance of the ELR (normalized to the half light radius of the galaxy). As this Figure shows, we see no indication for trend as a function of ELR location for either of the three types of ELGs we examine. A simple Pearsons linear correlation test for  $\text{H}\alpha$ , [OIII] and [OII] yields values of 0.04, -0.001 and -0.05, respectively, indicating no statistical correlation between location of ELRs and SFR in those ELRs.

Finally, Figure 15 compares Log SFR against Log  $M_*$  for the ELGs in the PEARS-2D sample (open circles in all panels). The ELGs are plotted in four redshift bins to match the work of Noeske et al. (2007). In that work Noeske et al. (2007) derived a “main-sequence” of star forming galaxies for field galaxies in the Extended Groth Strip, complete to Log  $M \sim 10.8$  (Figure 1 in that paper). The red squares shown in Figure 15 are the median values for the galaxies in Noeske et al. (2007) along with the  $\pm 1\sigma$  (dotted red line). The conclusion was that there exists a gradual decline in SF of most galaxies since  $z \sim 1$ . The implication is that the same physics that regulates SF in local disk galaxies is occurring, which could be either an evolution in the gas supply or changes in the SF efficiencies. Noeske et al. (2007) suggested that the slope of the “main-sequence” is related to the gas exhaustion of galaxies and is related to the age of the galaxy and SF timescale, all of which are dependent on the galaxy mass. The PEARS-2D sample probes galaxies to much lower masses than those in

Noeske et al. (2007). As such, we compare our galaxies to those in in Noeske et al. (2007) in Figure 15. From this we can conclude that the relation we observe between SFR and host galaxy stellar mass is consistent with the star formation "main sequence" of objects with stellar masses of  $\approx 10^{10} M_{\odot}$  while extending this relation by about four orders of magnitudes in mass. We also potentially witness a flattening of the sSFR versus mass relation for lower mass objects (below  $\approx 10^8 M_{\odot}$ ). The dashed horizontal lines in Figure 15 show our sensitivity limits at the lower and higher ends of the redshift ranges we show and it is clear that the flattening of this relation is not caused by incompleteness, especially at the higher redshifts.

## 4.2. The Host Galaxies

### 4.2.1. Morphologies

The PEARS-2D galaxies comprise a remarkably robust sample to test the evolution of ELGs and compare their morphologies with properties such as SFRs and stellar masses. Unlike many morphological studies, our sample was not pre-selected by redshift or luminosities. This sample serves as a random selection of star-forming galaxies within the PEARS redshift volume, which is mostly unbiased by the actual morphology of these star-forming galaxies. In this section, we parameterize the morphologies of the host galaxies using the Gini Coefficient  $G$  and  $M_{20}$  parameters (Lotz 2004). The  $G$  and  $M_{20}$  parameters can be thought of as proxies for clumpiness and concentration coefficients and have been shown to be a good way to distinguish between "normal" galaxies and galaxy mergers in the local Universe, as demonstrated by Lotz (2004) in the blue using Sloan  $g$ -band,  $B_J$ , Thuan-Gunn  $g$ , and  $B$ -band (all corresponding to  $(\approx 4300 - 4500 \text{ \AA})$ , as well as at  $\sim R$ -band. Local spiral and elliptical galaxies follow a well defined sequence (e.g. Figure 9 in Lotz (2004)), while mergers have larger  $G$  and smaller  $M_{20}$  values (Lotz 2004, 2008, 2010). In order to compare the PEARS ELGs to galaxies in general, we computed the rest-frame  $G$  and  $M_{20}$  coefficients for both the PEARS ELGs as well as the entire GOODS catalog using the GOODS 2.0 ACS public data. These values were measured in all available observed wavelengths and a  $\lambda \sim B$ -band (or  $\sim 4350 \text{ \AA}$ ) rest-frame value was obtained by linearly fitting these measurements.

As a comparison, we have also included field galaxies from within the same GOODS fields using the GOODS 2.0 ACS public data. For these objects, photometric redshifts were used to derive rest frame B band values for  $G$  and  $M_{20}$ . The rest-frame values of  $G$  and  $M_{20}$  were computed linearly fitting the values measured in each of the available bands. The galaxies are all plotted in Figure 16, which is divided into three rows of three panels for clarity. The field galaxies from GOODS are plotted as contours, and in each panel the  $H\alpha$  [OIII], and [OII] ELGs are shown separately. The solid lines in Figure 16 delineates disturbed

galaxies (above the line) from "normal" galaxies (below the line) according to Lotz (2004). We also show the regions containing early type and late type "normal" galaxies. When compared to the rest of the GOODS galaxies (black contours), the PEARS ELGs clearly have higher  $G$  and  $M_{20}$  values and fall above the fiducial line separating quiescent galaxies and active galaxies (from Lotz 2004). This strongly suggests that the PEARS ELGs have perturbed morphologies, likely due to galaxy interactions.

Figure 16 implies that the PEARS-2D ELGs have disturbed morphologies, likely from some type of interaction. We also see an indication that ELGs with more than one detected ELR tend to have more disrupted morphologies, as shown in the three panels in the middle row of Figure 16, while ELGs with a single ELR tend to lay closer to the line separating normal galaxies and mergers (bottom three panels), as defined by Lotz (2004). However, there is no correlation between the Gini- $M_{20}$  values and computed SFRs and stellar masses. To test for any correlation, the Pearson Correlation coefficient ( $r$ ) was used. It tests the degree of linear correlation between two independent data sets.  $r$  ranges in value from -1 to +1 (perfect negative or anti-correlation to perfect positive correlation). The most correlated relation we find is that of the [OIII] versus stellar mass, shown in Figure 17, which is very weak with a value of  $r = 0.16$ . All other relations show no statistical correlations.

#### 4.2.2. 4350Å Rest-frame Luminosity of ELGs

The underlying host galaxy luminosity may provide additional information about the nature of the ELGs and how they compare to other galaxies in the field. Absolute magnitudes at 4350Å ( $M_{4350}$ ) were computed for both the ELGs and GOODS field galaxies. Figure 18 shows a histogram distribution of  $M_{4350}$  for the ELGs, divided into three panels, one for emission line. The median  $M_{4350}$ s as a function of the emission line are: -21.2 for [OII]; -19.0 for [OIII]; and -18.2 for H $\alpha$ .

One important question is whether the ELGs are representative of other galaxies within the same volume. As discussed in the Introduction, ELGs are incredibly useful for probing the evolution of the SFR not only out to more distant epochs, but down to fainter luminosities (and thus lower masses) than other galaxies. Figure 19 compares the luminosity function of the ELGs (separated by emission line which, again, we point out approximates different redshift bins) compared with field galaxies from GOODS, also delineated by redshift. Figure 19 clearly shows that the maximum density of H $\alpha$ , [OIII], and [OII] occurs at much brighter levels than the depth of the GOODS data. While the luminosity functions of the GOODS field galaxies increases monotonically in a Schechter-like manner, the number of low mass line emitters decreases quickly. It is unlikely this trend is due to incompleteness. The PEARS-2D method is more sensitive to higher equivalent width lines, therefore we would expect to see

more emission lines with observed flux levels of  $3 \times 10^{-17}$  erg/s/cm<sup>2</sup> when the continuum light from host galaxies decreases. Yet, there appears to be an absence of faint emission line galaxies in all three sub-samples.

To further quantify the effect, we examined the volume densities of [OIII] emitting galaxies (our largest sample) at redshifts from 0 to 0.9. This is the redshift range with the largest number of ELGs. We imposed a further restriction and only selected galaxies above the completeness limit. This group was then divided into two subsets ( $0 < z < 0.5$  and  $0.5 < z < 0.9$ ) to see if the trend remained. The results are plotted in Figure 20 for  $M_{4350}$  (*left*) and Log Stellar Mass (*right*). The left panel of Figure 20 confirms that there appears to be a relatively small number of faint galaxies with detected [OIII] emission at higher redshifts. Recall that these host galaxies were selected solely based on the direct and independent detection of [OIII] in emission and thus independently of their observed size and host luminosity.

In the right panel of Figure 20 the stellar masses are compared for the two redshift ranges (same limits on sample selection as the left panel). The stellar mass distribution of galaxies with detected [OIII] emission differs significantly. At lower redshift there appears to be fewer massive galaxies with detected star formation. We conclude that, strongly star forming galaxies were on average more massive at higher redshifts. These results seem consistent with downsizing (Cowie et al. 1996, e.g.).

## 5. Conclusion

We have presented a sample of ELGs selected independently by their emission lines without *a priori* knowledge of their host properties. The methodology used (PEARS-2D) is based on *direct* detection of emissions line from *HST* slitless grism spectroscopy, with the added bonus of being able to detect multiple ELRs within a single galaxy. This has allowed us to construct a sample which is effectively random, and blind to other parameters. Using the wealth of ancillary data, we then investigated and compared the properties of the underlying hosts with the SFR histories derived from the ELRs. The key results are summarized below:

- 1) There is evidence for evolution in the luminosity function of  $H\alpha$ , [OIII] and [OII] emission lines. The slopes flatten as a function of redshift.
- 2) The morphology of the host galaxies clearly indicates that these objects are disturbed, although we detect no correlation between morphology and our stellar mass estimates, or star formation intensity.
- 3) The mass density function of [OIII] emitting galaxies at  $0 < z < 0.9$  strongly decreases. The number density of objects with stellar masses greater than  $\approx 10^{10} M_{\odot}$  undergoing strong

SF decreases at lower redshifts. This supports the idea of downsizing (Cowie et al. 1996, e.g.).

The results presented here also demonstrate the clear advantage of space-based grism spectroscopy using multiple position angles. Such observations are able to probe deeper than similar ground-based studies. The PEARS-2D method also provides a method for detecting multiple ELRs and allows spatial information about SF to be derived for galaxies. Future work will include using the WFC3 grism mode, with observed wavelength coverage of 0.8–1.6 $\mu\text{m}$ . This will allow us to probe to significantly higher redshifts and determine whether the trends reported here continue to earlier epochs.

*Acknowledgments* - NP wishes to thank Kai Noeske for the stimulating discussions. This research made use of the OSX version of SCISOFT assembled by Dr. Nor Pirzkal and F. Pierfederici.

Table 1. Summary of emission lines detected in the PEARs survey using the PEARs-2D method.

PEARs Field	R.A.	Dec.	No. PA <sup>a</sup>	Exposure (s) <sup>b</sup>	No. Objects	No. Knots	No. of lines										
							[OII]	[OIII]	H $\alpha$	CIV	CIII]	MgII	[NeIII]	H $\gamma$	Ly- $\alpha$	noID	All <sup>c</sup>
PEARs-N-1	189.1852503	+62.2032822	3	44708	153	167	48	73	26	5	6	6	1	5	2	1	173
PEARs-N-2	189.1877163	+62.2548588	3	44252	90	96	29	50	15	1	4	3	4	4	1	5	116
PEARs-N-3	189.3100669	+62.2924237	3	44708	98	104	33	43	16	5	9	5	1	2	1	2	117
PEARs-N-4	189.3720309	+62.3201389	3	44708	91	98	23	42	35	1	10	3	0	2	1	6	123
PEARs-S-HUDF	53.16231255	-27.7911063	4	89819	152	166	46	61	40	7	7	13	0	3	2	14	193
PEARs-S-1	53.16967450	-27.9014641	3	43733	54	61	10	34	28	0	0	0	0	2	0	2	76
PEARs-S-2	53.17745315	-27.8416506	4	51583	52	54	20	40	5	0	0	0	1	2	0	2	70
PEARs-S-3	53.11987485	-27.7396665	3	44186	112	127	29	59	34	0	6	5	1	3	1	7	145
PEARs-S-4	53.06664343	-27.7088154	4	44084	123	131	31	62	20	3	4	9	2	6	3	9	149
PEARs-N <sup>d</sup>					417	451	133	208	92	12	29	17	6	13	5	14	529
PEARs-S <sup>e</sup>					489	535	136	256	127	10	17	27	4	16	6	34	633
PEARs TOTAL <sup>f</sup>					906	986	269	464	219	22	46	44	10	29	11	48	1162

Note. — (a) Number of orientations at which this field was observed.

(b) Total exposure time (in s) of all the data obtained for this field, including all orientations.

(c) Includes Ly- $\alpha$ , CIV, CIII], MgII, [OII], [NeIII], [OIII], H $\gamma$ , and H $\alpha$ .

(d) Sum for all the PEARs-N fields.

(e) Sum for all the PEARs-S fields.

(g) Sum for all of the PEARs fields.

Table 2. Properties of PEARs Emission-Line Galaxies.

PEARs Field	PEARs ID	PEARs ELR ID	R.A. (deg)	DEC (deg)	Grism Redshift	Flux ( $10^{-18} \text{ erg/s/cm}^2$ )	Wavelength (Å)	EW (Å)	$i_{AB}$ (mag)	Line ID	Line Grade
PEARs-N-1	n39842	2	189.18321221	62.18527049	0.85	$108.6 \pm 19.4$	9275	289	22.6	[OIII]	3.7
PEARs-N-1	n40322	1	189.17999436	62.18558444	0.30	$31.8 \pm 14.0$	6462	176	24.0	[OIII]	2.8
PEARs-N-1	n40322	1	189.17999436	62.18558444	0.30	$16.3 \pm 4.4$	8552	57	24.0	H $\alpha$	3.4
PEARs-N-1	n40498	1	189.15281320	62.18651377	0.85	$47.4 \pm 2.3$	6895	94	23.0	[OII]	4.0
PEARs-N-1	n40498	1	189.15281320	62.18651377	0.85	$121.7 \pm 53.1$	9257	297	23.0	[OIII]	3.7
PEARs-N-1	n40498	2	189.15281320	62.18651377	0.86	$58.9 \pm 18.1$	9281	134	23.0	[OIII]	3.4
PEARs-N-1	n40538	1	189.15448107	62.18661590	0.94	$28.9 \pm 18.2$	7251	176	23.1	[OII]	3.7
PEARs-N-1	n40833	1	189.20594162	62.18689331	0.46	$23.6 \pm 1.6$	7290	115	23.3	[OIII]	3.1
PEARs-N-1	n41172	1	189.17296602	62.18743270	0.51	$23.5 \pm 6.5$	7571	111	24.2	[OIII]	3.5
PEARs-N-1	n41339	2	189.17336461	62.19212062	0.10	$38.7 \pm 29.8$	7191	24	19.6	H $\alpha$	2.2
PEARs-N-1	n41339	3	189.17336461	62.19212062	0.14	$299.3 \pm 32.0$	7236	185	19.6	H $\alpha$	2.7

Note. — This table is available in its entirety in the online journal. A portion of it is shown here.

Table 3. Luminosity Function

Method	Line	Redshift Range	PEARS-N			PEARS-S			PEARS		
			$L_*$	$\alpha$	$\Phi_*$	$L_*$	$\alpha$	$\Phi_*$	$L_*$	$\alpha$	$\Phi_*$
STY	[OII]	$0.5 < z < 1.6$	$42.39^{+3.11}_{-0.27}$	$-2.37^{+0.15}_{-0.19}$	$-4.75^{+0.39}_{-4.89}$	$42.33^{+3.15}_{-0.34}$	$-2.36^{+0.16}_{-0.18}$	$-4.77^{+0.28}_{-5.74}$	$42.36^{+3.31}_{-0.43}$	$-2.36^{+0.10}_{-0.15}$	$-4.77^{+0.28}_{-5.58}$
	[OIII]	$0.1 < z < 0.9$	$41.62^{+0.21}_{-0.27}$	$-1.57^{+0.20}_{-0.13}$	$-2.99^{+0.31}_{-0.29}$	$42.79^{+2.56}_{-0.31}$	$-1.76^{+0.10}_{-0.13}$	$-4.21^{+0.28}_{-2.82}$	$42.43^{+3.32}_{-0.44}$	$-1.75^{+0.13}_{-0.16}$	$-3.89^{+0.55}_{-3.27}$
	H $\alpha$	$0.0 < z < 0.5$	$42.17^{+3.07}_{-0.48}$	$-1.58^{+0.12}_{-0.20}$	$-3.45^{+0.39}_{-2.79}$	$41.25^{+0.99}_{-0.30}$	$-1.50^{+0.14}_{-0.23}$	$-2.74^{+0.35}_{-1.11}$	$41.77^{+2.85}_{-0.25}$	$-1.58^{+0.05}_{-0.22}$	$-3.20^{+0.17}_{-2.54}$
$1/V_{\max}$	[OII]	$0.5 < z < 1.6$	$44.00^{+0.00}_{-0.00}$	$-1.89^{+0.20}_{-0.19}$	$-6.07^{+0.46}_{-0.68}$	$44.00^{+0.00}_{-0.00}$	$-2.16^{+0.19}_{-0.21}$	$-6.89^{+0.47}_{-0.67}$	$43.74^{+0.26}_{-1.29}$	$-1.96^{+0.11}_{-0.08}$	$-6.02^{+1.39}_{-0.49}$
	[OIII]	$0.10 < z < 0.90$	$41.13^{+0.15}_{-0.13}$	$-1.32^{+0.12}_{-0.14}$	$-2.48^{+0.16}_{-0.23}$	$41.76^{+0.50}_{-0.39}$	$-1.45^{+0.15}_{-0.10}$	$-3.01^{+0.27}_{-0.73}$	$41.64^{+0.20}_{-0.20}$	$-1.52^{+0.09}_{-0.08}$	$-2.98^{+0.20}_{-0.26}$
	H $\alpha$	$0.00 < z < 0.49$	$41.47^{+0.72}_{-0.47}$	$-1.62^{+0.08}_{-0.08}$	$-3.12^{+0.34}_{-1.94}$	$41.19^{+0.21}_{-0.19}$	$-1.40^{+0.10}_{-0.09}$	$-2.69^{+0.20}_{-0.23}$	$41.10^{+0.17}_{-0.10}$	$-1.44^{+0.06}_{-0.06}$	$-2.61^{+0.12}_{-0.17}$



Table 4. Properties of significantly detected (grade>2.5) emission lines in the PEARS sample

Line	Number Detected	$\langle z \rangle$	Flux (erg/s/cm <sup>2</sup> )	
			Average	Median
H $\alpha$	174	0.26	$9.44 \times 10^{-16}$	$5.54 \times 10^{-17}$
[OIII]	401	0.54	$9.65 \times 10^{-17}$	$4.13 \times 10^{-17}$
[OII]	167	0.91	$4.19 \times 10^{-17}$	$2.49 \times 10^{-17}$

Table 5. PEARs Luminosity Function  $H\alpha$  Estimates as a Function of Redshift

[OII]		[OIII]		$H\alpha$	
Redshift Range	$\alpha$	Redshift Range	$\alpha$	Redshift Range	$\alpha$
$0.47 < z < 0.97$	$-0.98^{+0.98}_{-1.25}$	$0.10 < z < 0.56$	$-1.79^{+0.14}_{-0.17}$	$0.00 < z < 0.27$	$-2.02^{+0.09}_{-0.09}$
$0.97 < z < 1.63$	$0.00^{+0.00}_{-1.09}$	$0.56 < z < 0.90$	$-0.86^{+0.86}_{-0.61}$	$0.27 < z < 0.49$	$-1.11^{+0.21}_{-0.25}$
$0.47 < z < 0.85$	$-1.66^{+1.66}_{-0.75}$	$0.10 < z < 0.45$	$-2.34^{+0.19}_{-0.12}$	$0.00 < z < 0.21$	$-2.12^{+0.14}_{-0.15}$
$0.85 < z < 1.18$	$0.00^{+0.00}_{-2.74}$	$0.45 < z < 0.65$	$-1.21^{+0.24}_{-0.73}$	$0.21 < z < 0.33$	$-1.32^{+0.24}_{-0.30}$
$1.18 < z < 1.63$	$-0.33^{+0.33}_{-1.43}$	$0.65 < z < 0.90$	$0.00^{+0.00}_{-1.14}$	$0.33 < z < 0.49$	$-0.98^{+0.28}_{-0.61}$

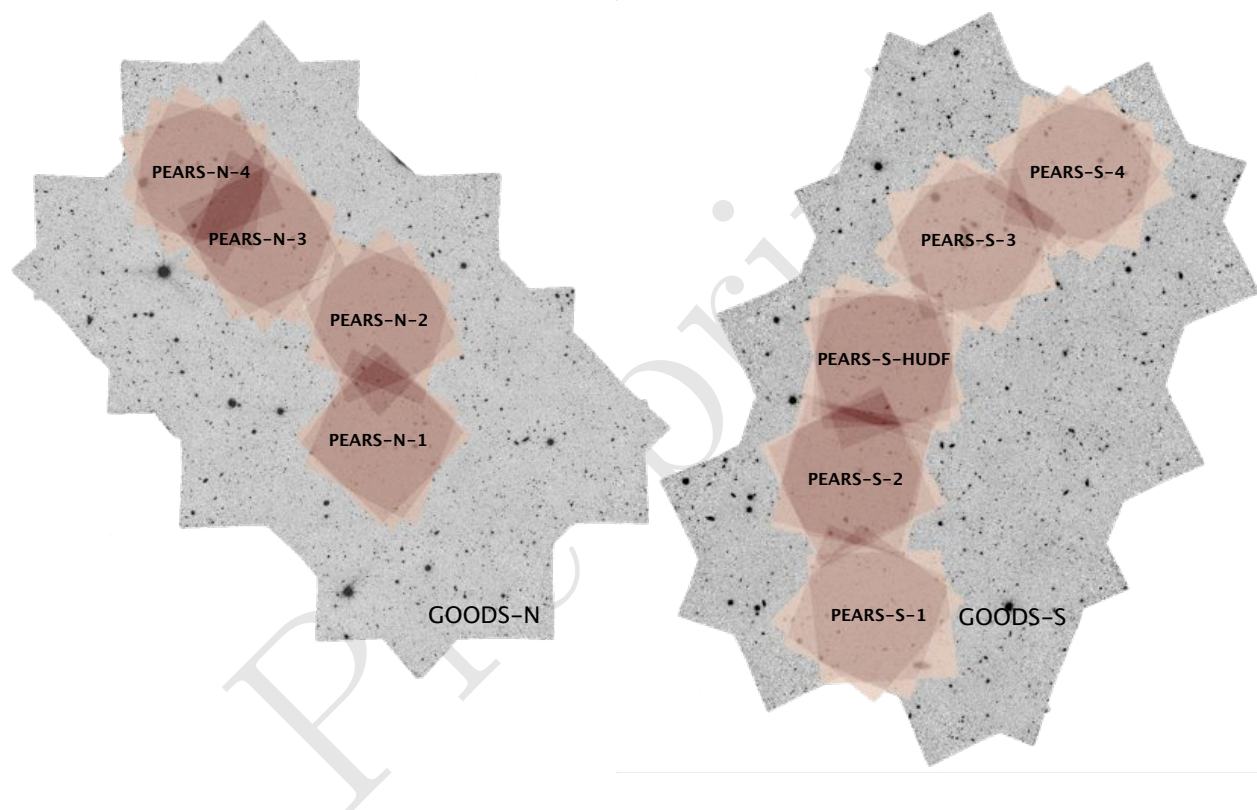


Fig. 1.— The location of the four PEARs-N (left) and five PEARs-S fields (right) within the GOODS-N and GOODS-S fields. The fields are oriented so that North is up and East is to the left. Each of the shown PEARs field is approximately 200'' arc second wide. Note that the total area where PEARs fields overlap is higher in PEARs-N than in PEARs-S.

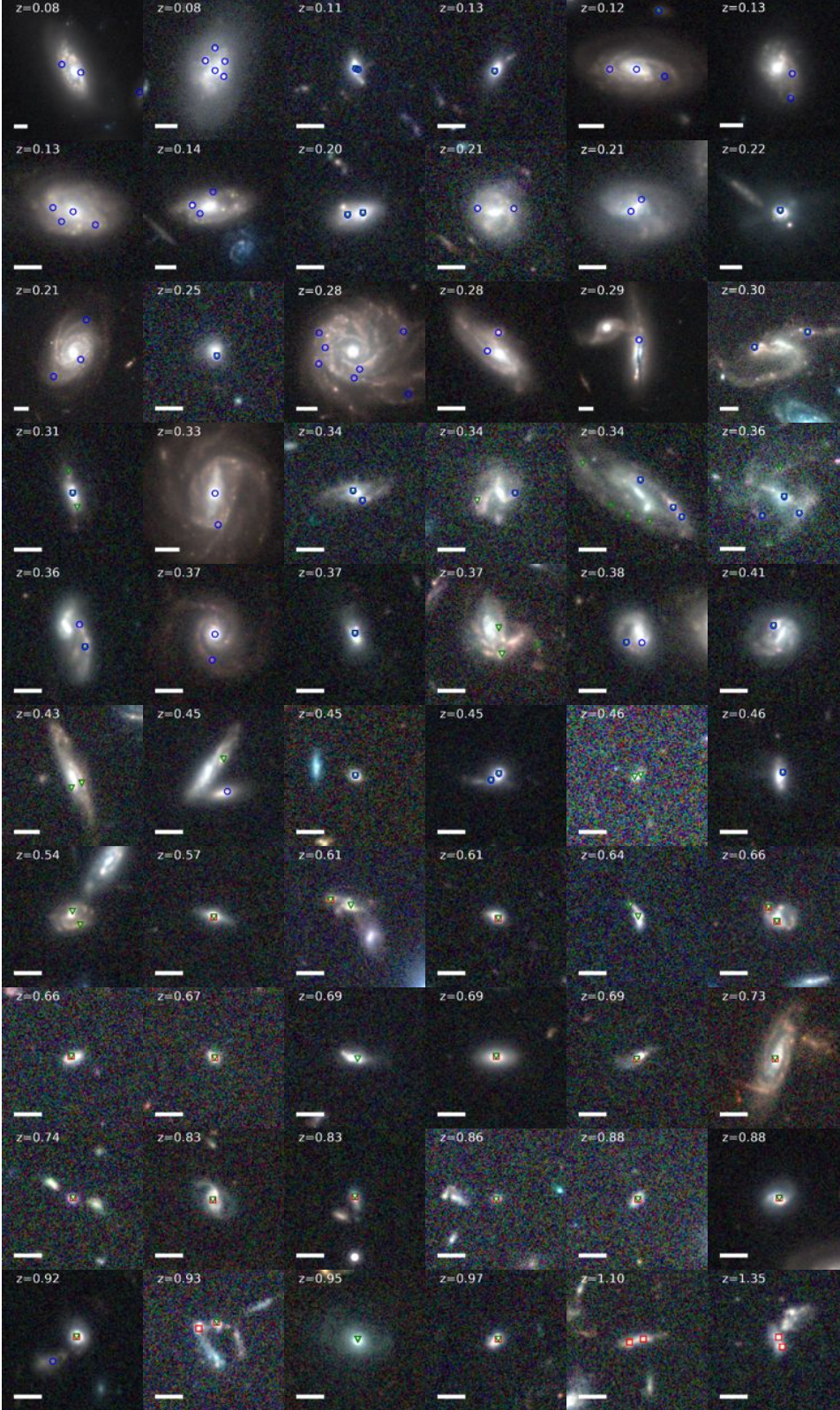


Fig. 2.— A sample of PEARS star forming galaxies with their identified star forming regions by red squares ([OII]), green triangles ([OIII]), and blue circles ( $H\alpha$ ). The redshift is indicated at the top left of each stamp image and the one arc second scale is shown at the bottom left of each stamp images.

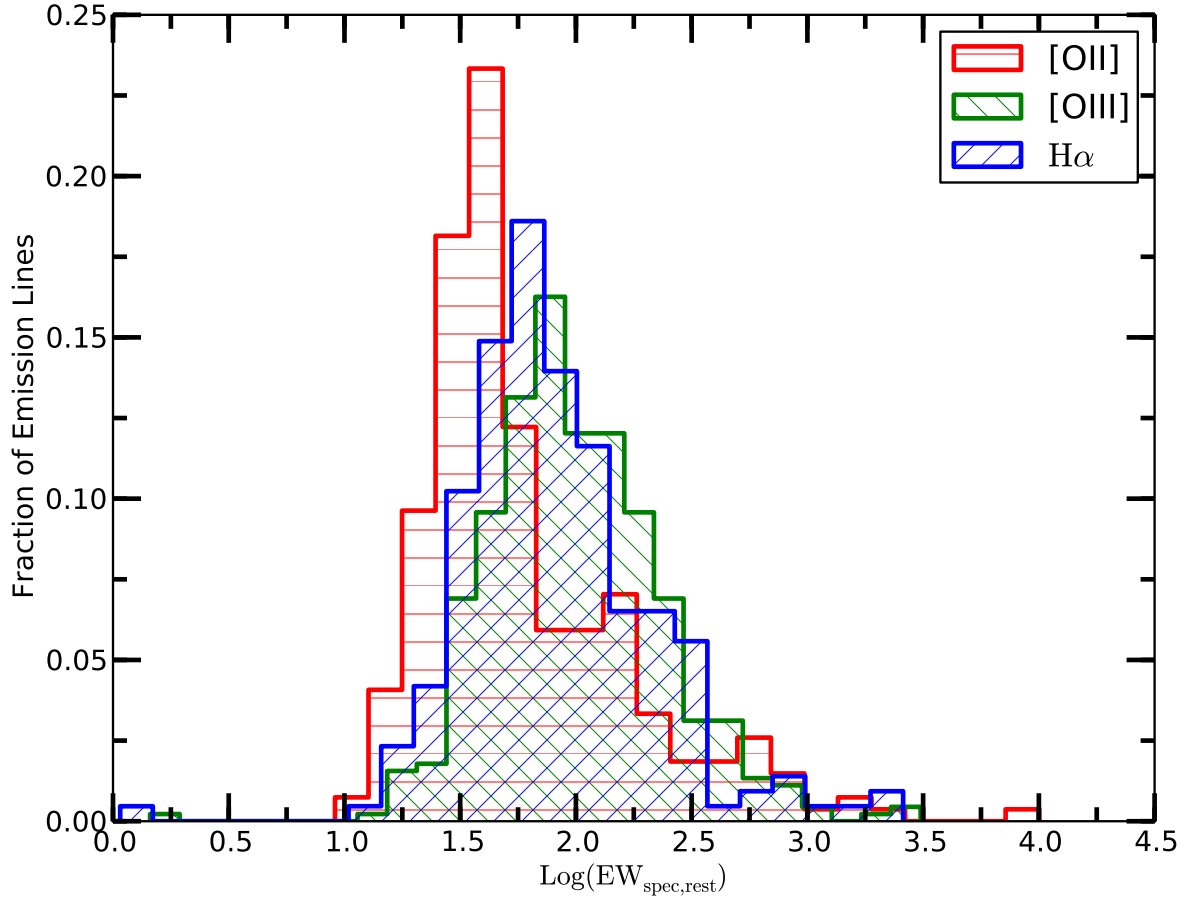


Fig. 3.— Rest-frame spectroscopic EW in the PEARS-2D sample. The median EW<sub>spec</sub> we measure are 43Å, 89Å, and 69Å for [OII], [OIII], and Hα emission lines, respectively. These lines act as proxies for the redshift ranges of  $0 < z < 0.5$ ,  $0.1 < z < 0.9$ , and  $0.5 < z < 1.5$ , respectively.

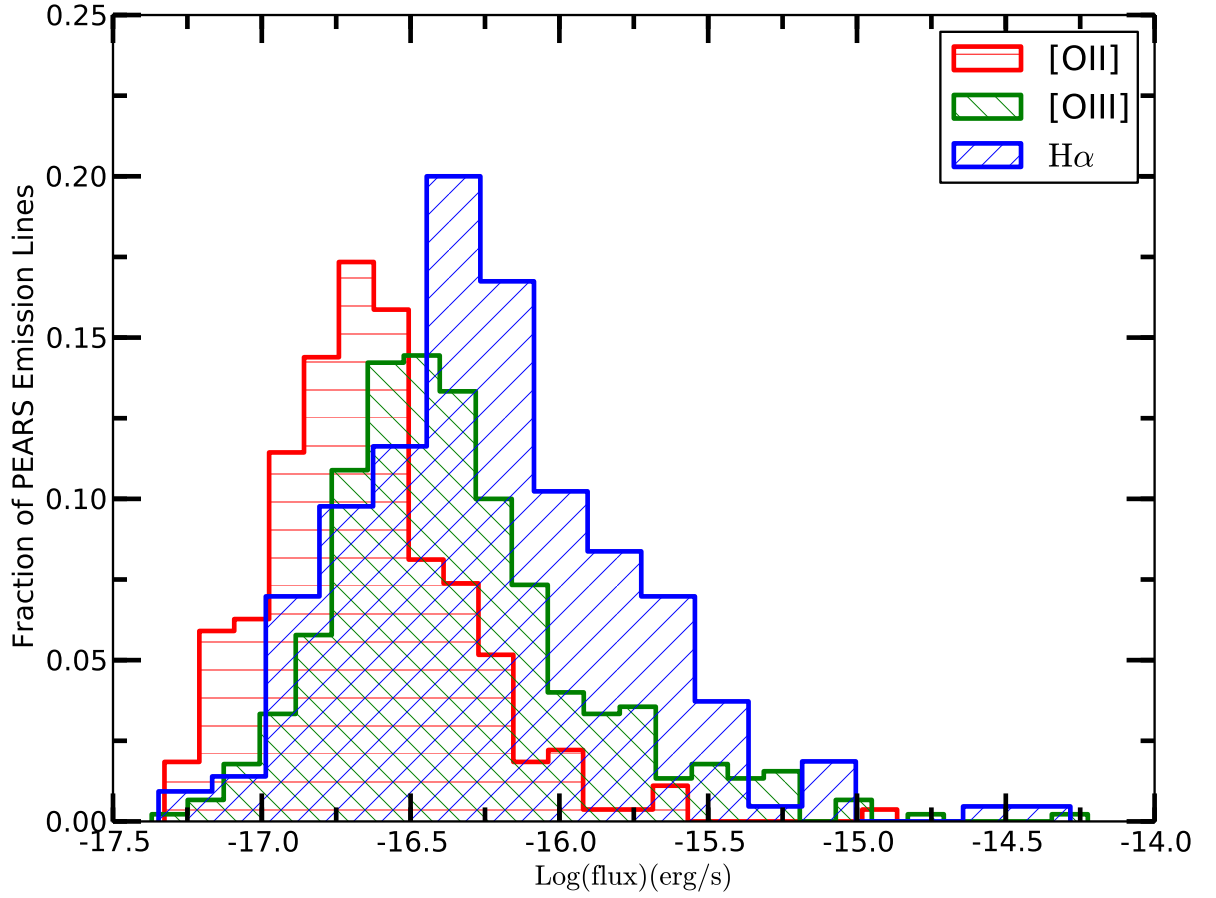


Fig. 4.— Distributions of observed line fluxes in the PEARS-2D sample, uncorrected for completeness or dust extinction. These lines act as proxies for the redshift ranges of  $0 < z < 0.5$ ,  $0.1 < z < 0.9$ , and  $0.5 < z < 1.5$ , respectively.

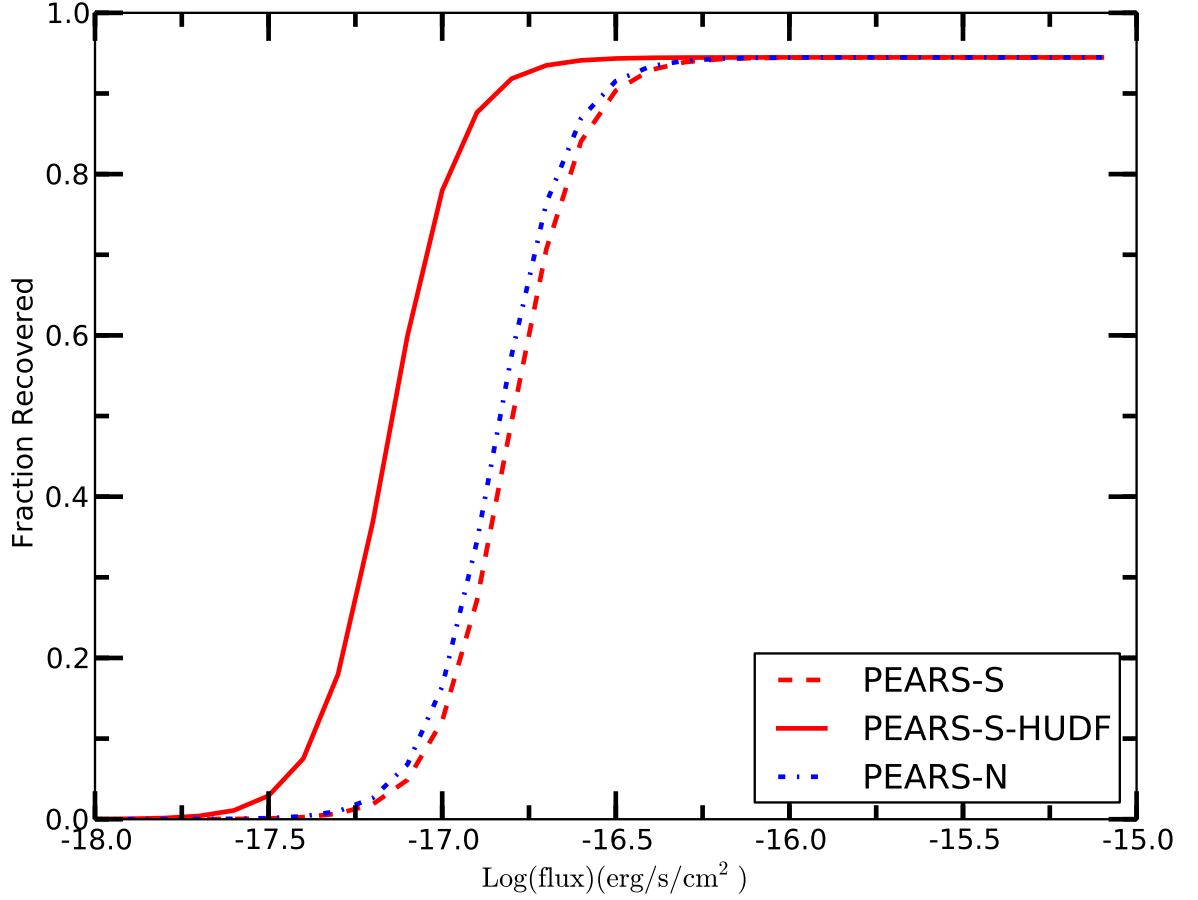


Fig. 5.— PEARS sensitivity to emission line flux. Based on our simulations, we estimate that we can reliably detect emission lines with fluxes greater than  $3 \times 10^{-17} \text{ erg/s/cm}^2$  over the whole PEARS fields while the PEARS-S-HUDF field, which was observed twice as long as each of the other 8 fields, reaches line fluxes approximately 1.4 times fainter.

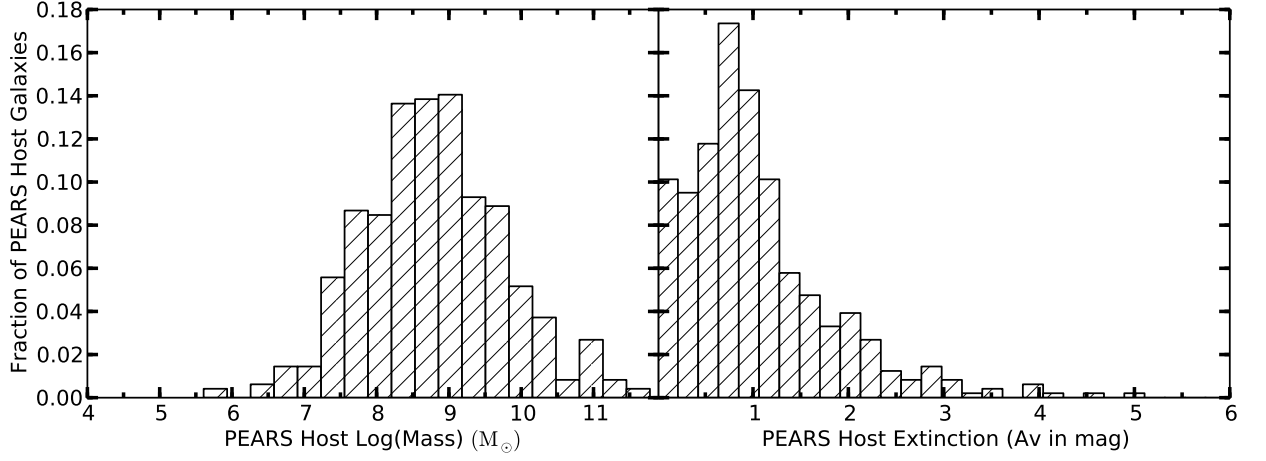


Fig. 6.— Left panel: Histogram of the PEARS emission line galaxies stellar masses (in  $M_{\odot}$ ) as determined from SED fitting. We derive a mean stellar mass of  $\text{Log}(\text{mass}) = 8.74 \pm 0.97 M_{\odot}$ . Right panel: Histogram of the PEARS emission line galaxies extinction ( $A_v$  in mag) as determined from SED fitting. We derive a mean extinction of  $A_v = 0.87 \pm 0.88$  mag



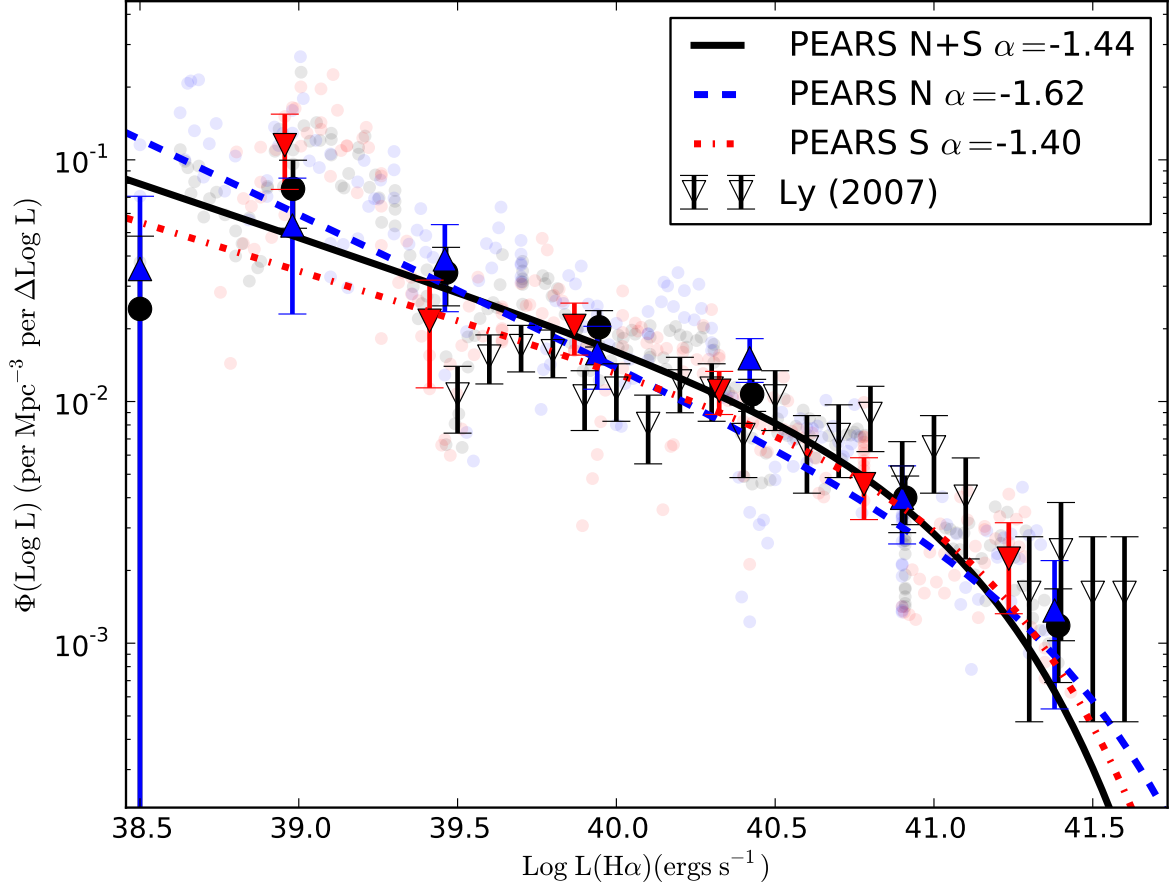


Fig. 7.— PEARS  $H\alpha$  luminosity function at  $0 < z < 0.5$ . We show the  $1/V_{\max}$  results for the full PEARS, PEARS-N and PEARS-S in black circles, blue upright triangles, and red downward triangles, respectively. The fits to the  $1/V_{\max}$  results are shown by the solid black line, blue dashed line, and red dash-dotted line, for PEARS, PEARS-N and PEARS-S. We see no significant differences between the PEARS-N and PEARS-S fields. We also plot the sample of  $z = 0.4$   $H\alpha$  emitters from Ly et al. (2007), also with no dust correction and excluding objects with  $EW < 50\text{\AA}$  from their sample so that we can better compare our results and demonstrate how PEARS reaches down to fainter luminosities.

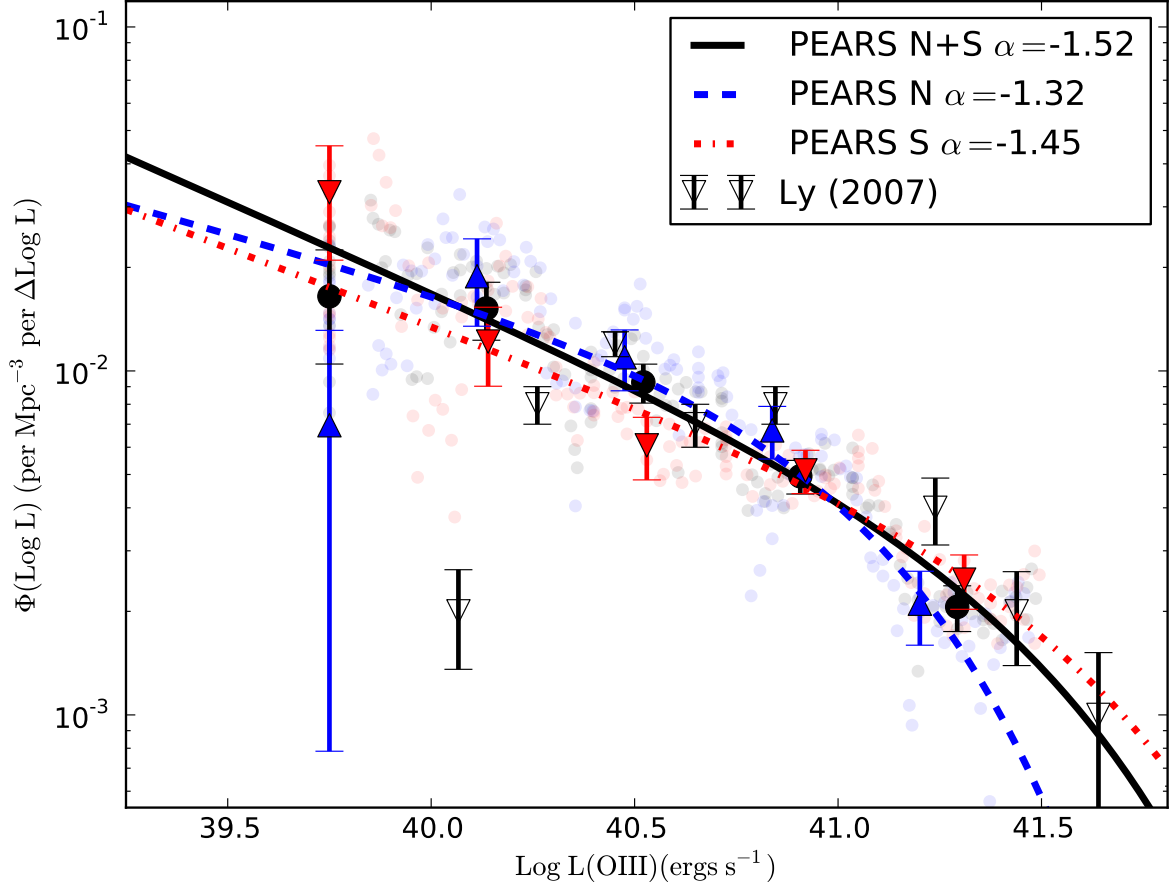


Fig. 8.— PEARS [OIII] luminosity function at  $0.1 < z < 0.9$ . We show the  $1/V_{\text{max}}$  results for the full PEARS, PEARS-N and PEARS-S in black circles, blue upright triangles, and red downward triangles, respectively. The fits to the  $1/V_{\text{max}}$  results are shown by the solid black line, blue dashed line, and red dash-dotted line, for PEARS, PEARS-N and PEARS-S. We see no significant differences between the PEARS-N and PEARS-S fields. We also plot the sample of  $z = 0.6$  [OIII] emitters from Ly et al. (2007), also with no dust correction and excluding objects with  $\text{EW} < 50\text{\AA}$  from their sample so that we can better compare our results and demonstrate how PEARS reaches down to fainter luminosities.

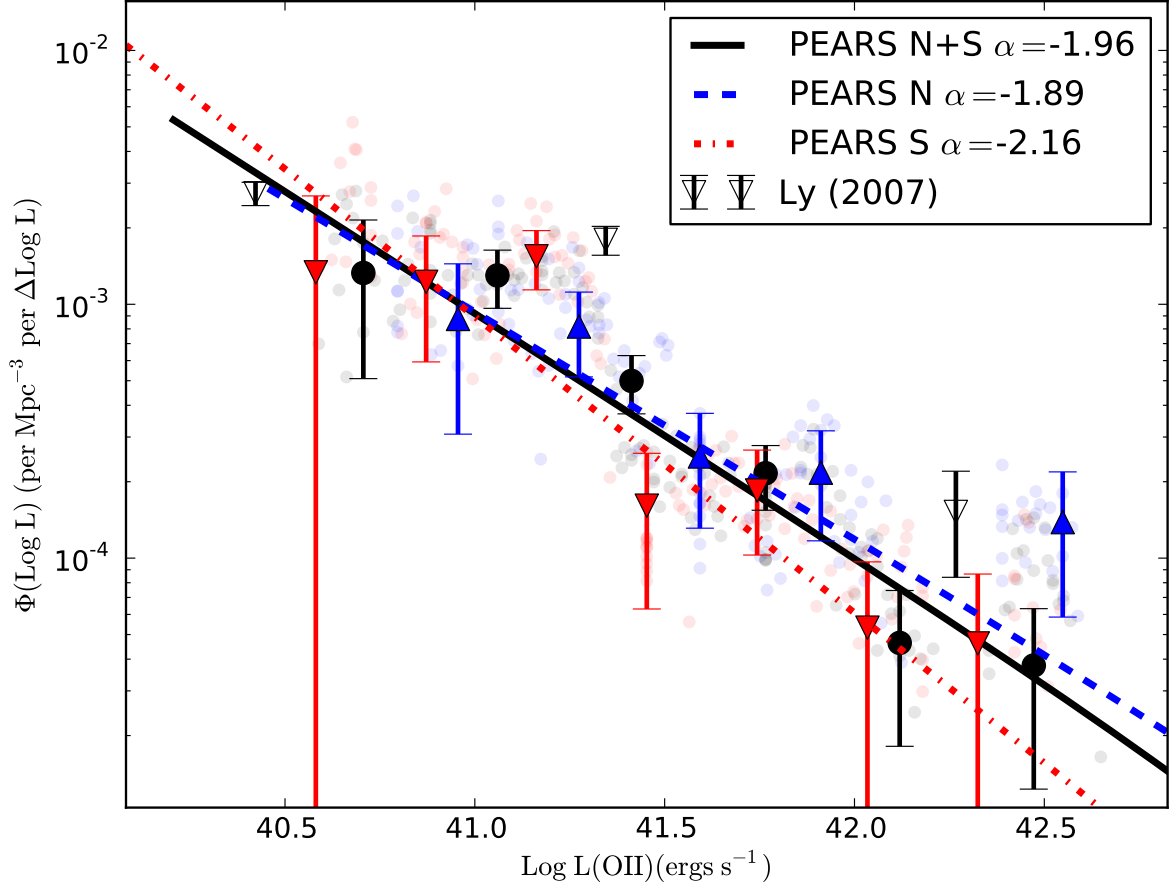


Fig. 9.— PEARS [OII] luminosity function at  $0.9 < z < 1.5$ . We show the  $1/V_{\text{max}}$  results for the full PEARS, PEARS-N and PEARS-S in black circles, blue upright triangles, and red downward triangles, respectively. The fits to the  $1/V_{\text{max}}$  results are shown by the solid black line, blue dashed line, and red dash-dotted line, for PEARS, PEARS-N and PEARS-S. We detect no significant differences between the PEARS-N and PEARS-S fields. We also plot the sample of  $z = 0.9$  [OII] emitters from Ly et al. (2007), also with no dust correction and excluding objects with  $\text{EW} < 50\text{\AA}$  from their sample so that we can better compare our results.

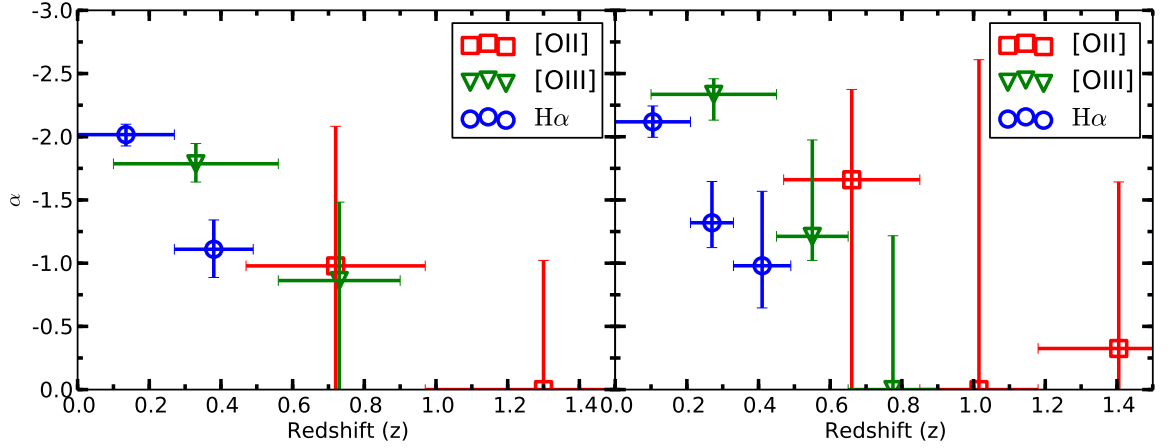


Fig. 10.— Slope of the PEARs [OII], [OIII], and H $\alpha$  luminosity functions as a function of redshift. In the left panel, each set of emission lines is split into two groups of redshift ranges (yielding 6 bins). This shows a clear trend in which the slope ( $\alpha$ ) decreases with increasing redshift. In the right panel, each set of emission lines was divided into three redshift bins (yielding 9 bins in total). Again, the trend remains present. We present both a two and a three bins solution to show that the trend we show is not strongly affected by the binning.

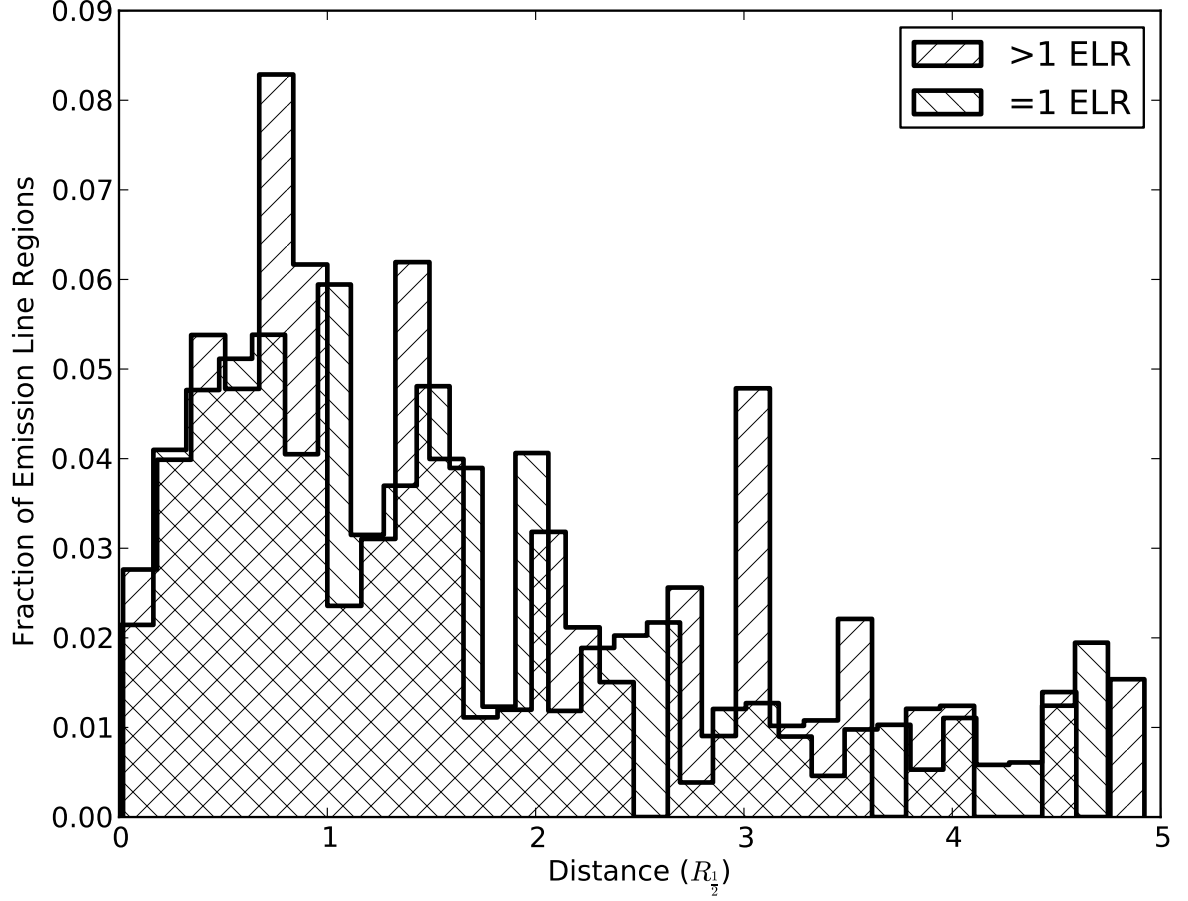


Fig. 11.— Histograms of the distance of the PEARS ELRs from the center of their host galaxies, measured in units of multiple  $R_{\frac{1}{2}}$ . We show the distribution of ELRs in ELGs where only one ELR was identified as well as the distribution of ELRs in ELGs where more than one ELR was identified. There is no evidence that these distributions are different and a K-S test p-value of 0.49 confirms this.

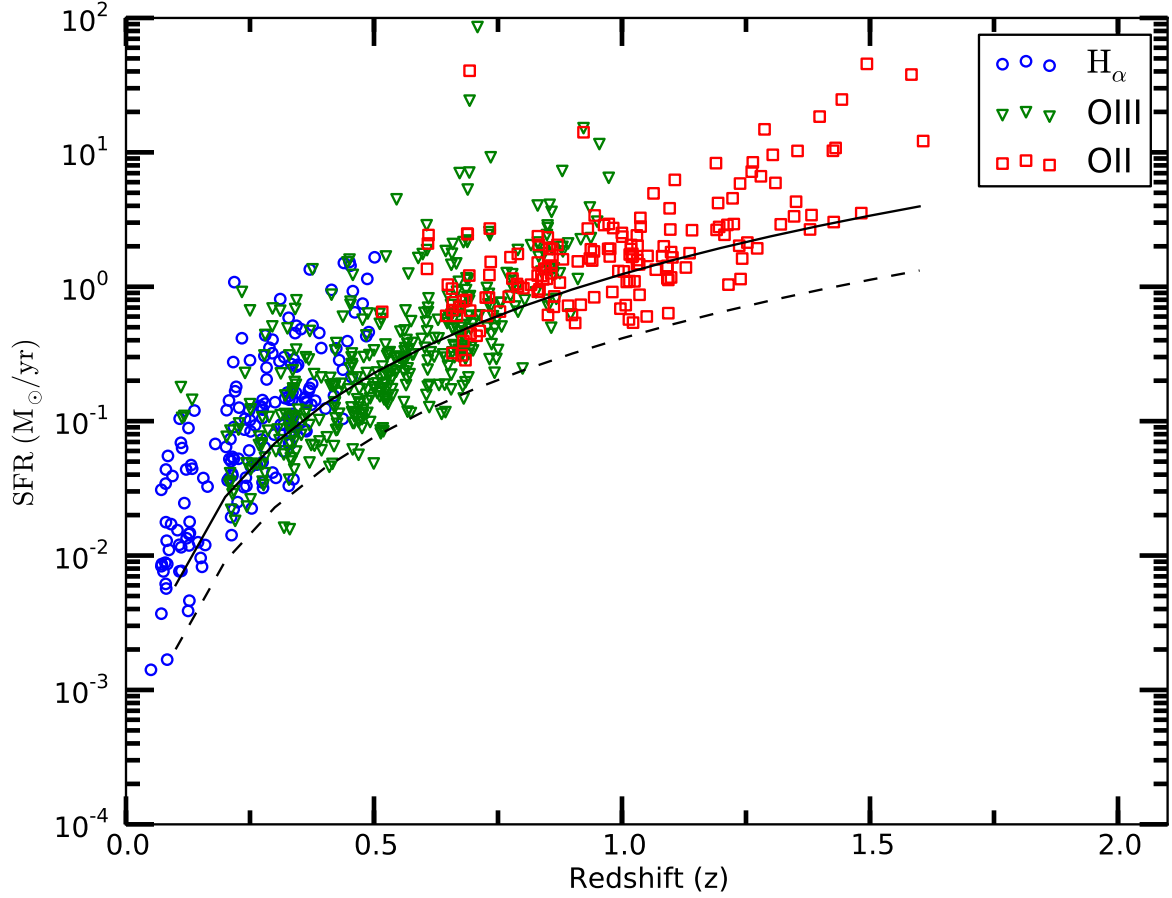


Fig. 12.— SFR as a function of redshift for the PEARS  $[OII]$   $[OIII]$  and  $H\alpha$  sources with a line grade greater than 2.5. The solid black line shows the SFR corresponding to a flux limit ( $\approx 80\%$  completeness limit) of  $3 \times 10^{-17} \text{ erg/s/cm}^2$ . The dashed black line corresponds to an emission line flux of  $1 \times 10^{-17} \text{ erg/s/cm}^2$

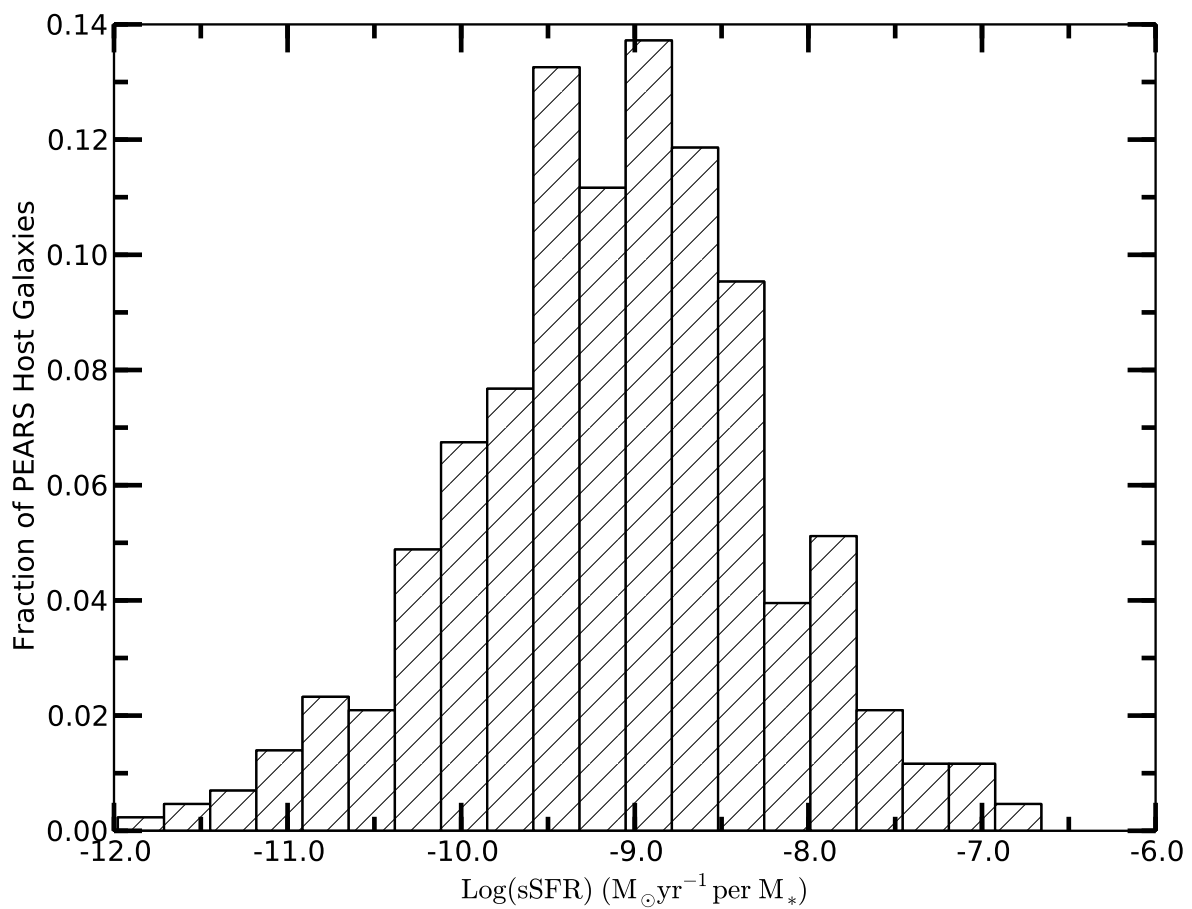


Fig. 13.— Distribution of sSFR for the PEARs host galaxies.

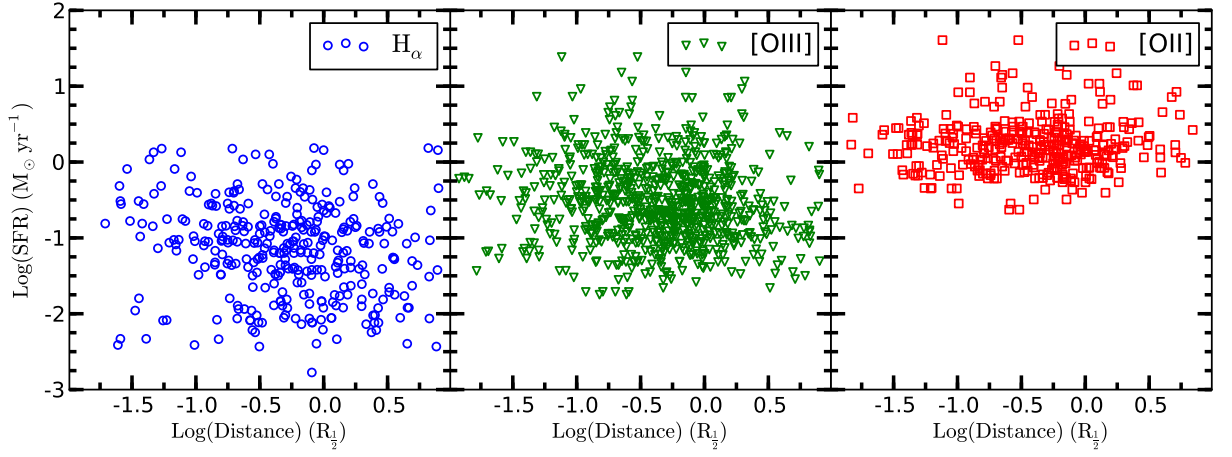


Fig. 14.— SFR of the PEARS emission line regions plotted as a function of their radial position in their host galaxy, normalized to the half light radius of the host galaxy). The amount of star formation appears completely uncorrelated to the location of the ELR in the host galaxy with Pearsons correlation coefficients of -0.001, -0.05 and 0.04 for  $\text{H}\alpha$ ,  $[\text{OIII}]$  and  $[\text{OII}]$ , respectively. These three panels are proxies for the redshift bins of  $0 < z < 0.5$ ,  $0.1 < z < 0.9$ , and  $0.5 < z < 1.5$ , respectively.



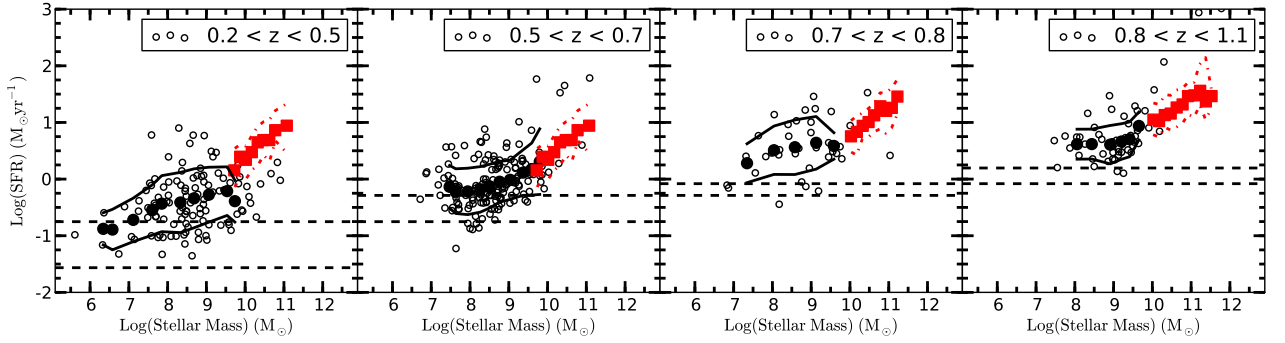


Fig. 15.— Comparison of SFR with Stellar Mass for the ELG sample (open black circles). The data have been binned into 4 redshift ranges for 1:1 comparison with higher mass star forming galaxies from the Extended Groth Strip (Noeske et al. 2007). The dash-dotted red line represents the  $\pm 1\sigma$  of the median values. The solid black circles represents the median for the ELG sample. The solid black lines represents the  $\pm 1\sigma$  of the median values. The dashed horizontal line represents the 80% completion levels at the minimum and maximum redshifts considered in each panel.

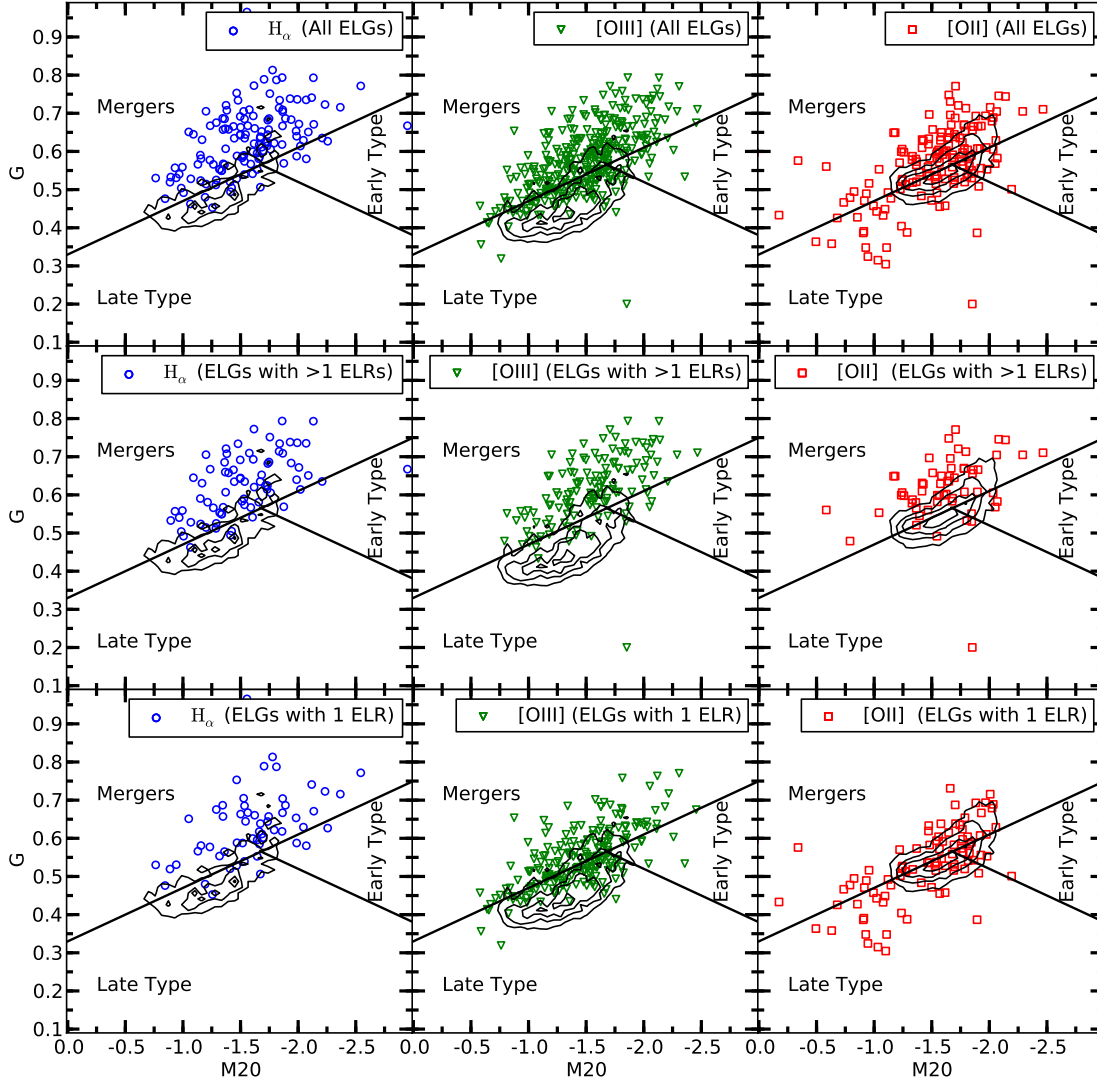


Fig. 16.— Morphology of the PEARs ELGs as parametrized by the Gini and M20 coefficients at the rest-frame wavelength of 4350Å. Top row: PEARs ELGs with [OII], [OIII], and H $\alpha$  ELRs (red square, green triangle and blue circle, left to right columns, respectively). Middle row: PEARs ELGs containing multiple ELRs. Bottom row: PEARs ELGs containing only one ELR. In every panel we show the rest-frame morphology of the GOODS field galaxies with photometric redshift estimates that are within the appropriate redshift ranges  $0 < z < 0.5$ ,  $0.1 < z < 0.9$ , and  $0.5 < z < 1.5$ , left to right columns, respectively. The hosts of the emission lines we detected are nearly all above the line (shown in black) separating “normal” galaxies (below the line) and “merging” galaxies in the nearby Universe and is taken from Lotz (2004).

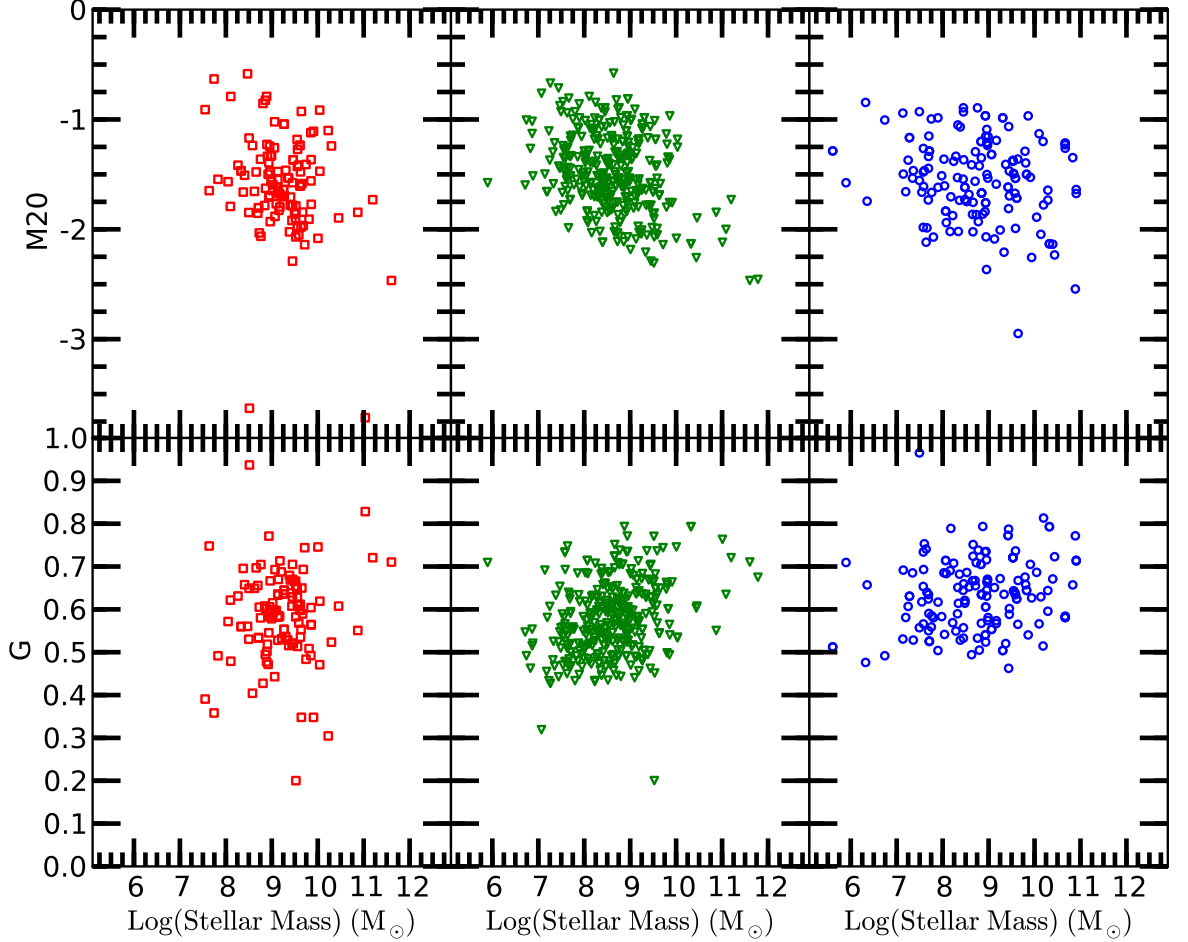


Fig. 17.— Gini coefficient values of the PEARs host galaxies versus their stellar masses, as estimated from SED fitting. The M20 and the Gini values are shown in the top and bottom row, respectively. We also show the  $H\alpha$ , [OIII] and [OII] host galaxies separately in the left, middle and right most column respectively. There is little evidence for a strong trend between stellar mass and either the M20 or Gini coefficients in our PEARs emission line host galaxies, as indicated by Pearsons correlation coefficient values of at most  $\approx 0.16$ . However, a mild decrease in M20 and increase in the Gini coefficient as stellar mass increases can be seen for the [OIII] and  $H\alpha$  host galaxies (at redshifts of  $0.1 < z < 0.9$  and  $0 < z < 0.5$  respectively).

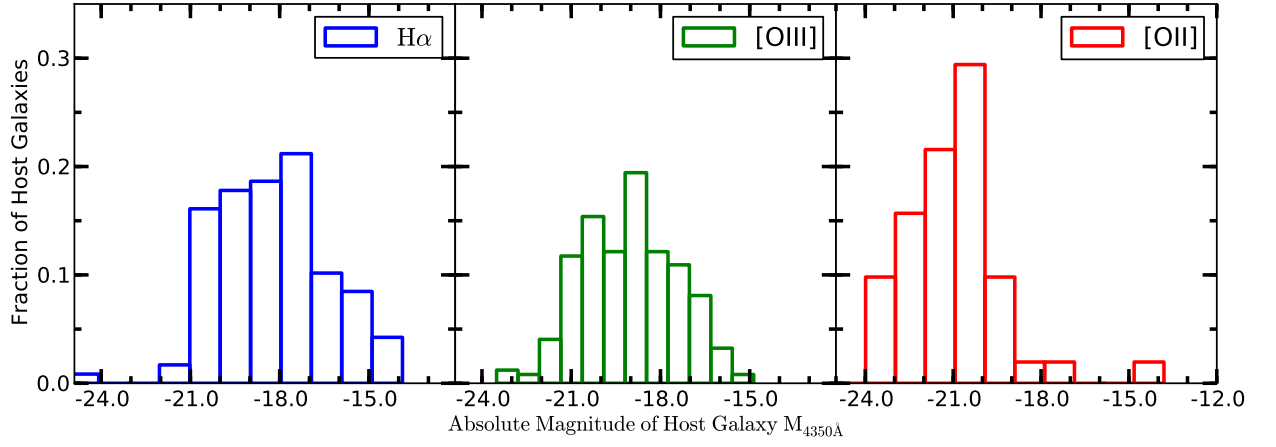


Fig. 18.— Distributions of the 4350Å rest-frame absolute magnitude of the host galaxies of the PEARS H $\alpha$ , [OIII] and [OII] emission line (redshift ranges of  $0 < z < 0.5$ ,  $0.1 < z < 0.9$ , and  $0.5 < z < 1.5$ , respectively).

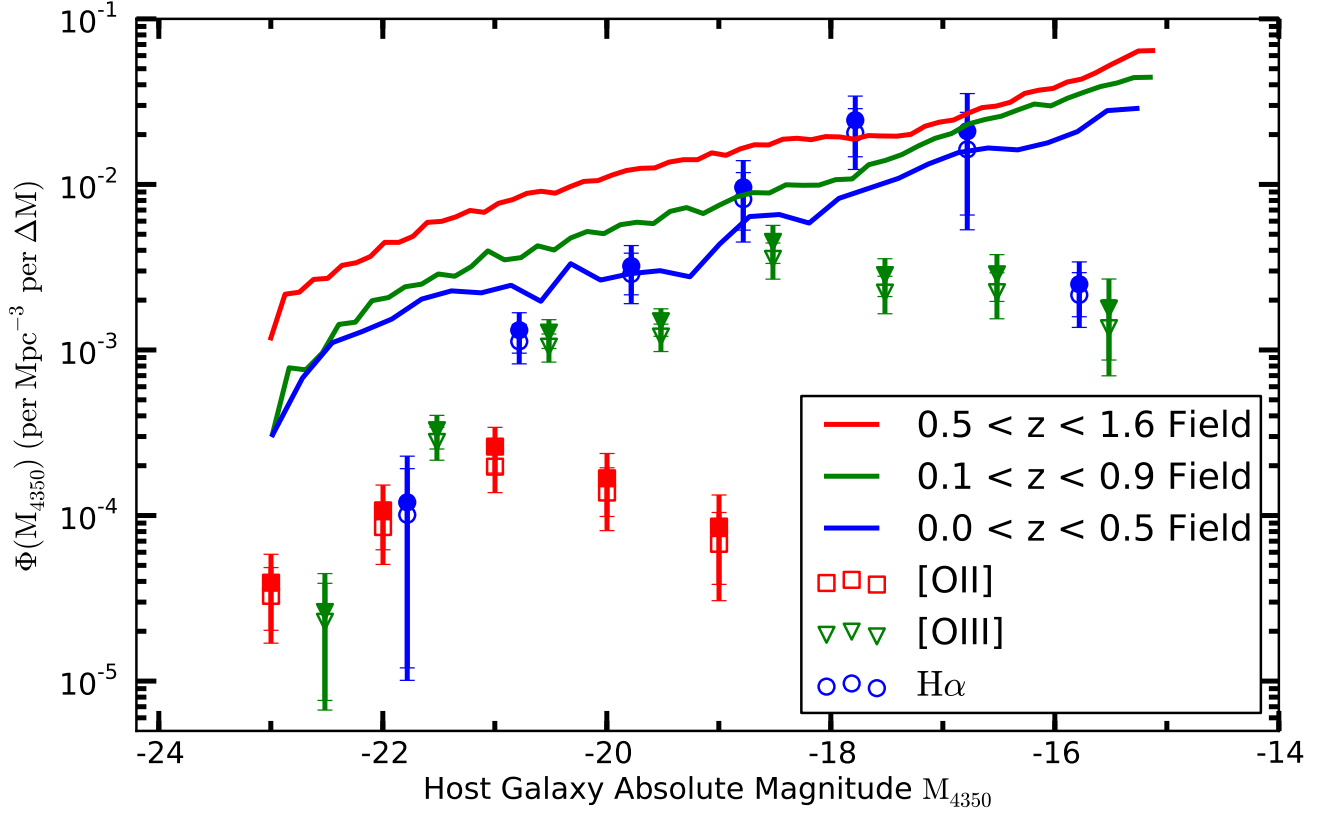


Fig. 19.— Luminosity functions of the 4350Å rest-frame absolute magnitude of the host galaxies of the PEARS H $\alpha$ , [OIII] and [OII] emission line (symbols with error bars, redshift ranges of  $0 < z < 0.5$ ,  $0.1 < z < 0.9$ , and  $0.5 < z < 1.5$ , respectively). The luminosity function of GOODS field galaxies at respectively similar redshifts are shown (scaled) using solid lines. The density of H $\alpha$  emitters ( $0 < z < 0.5$ ) peaks at  $\approx -18$ , while the density of [OIII] emitters peaks at  $\approx -19$  and the density of [OII] emitting galaxies ( $0.5 < z < 1.6$ ) peaks at  $\approx -21$ . We show both the completeness corrected (filled symbols) and uncorrected (open symbols) density estimates.

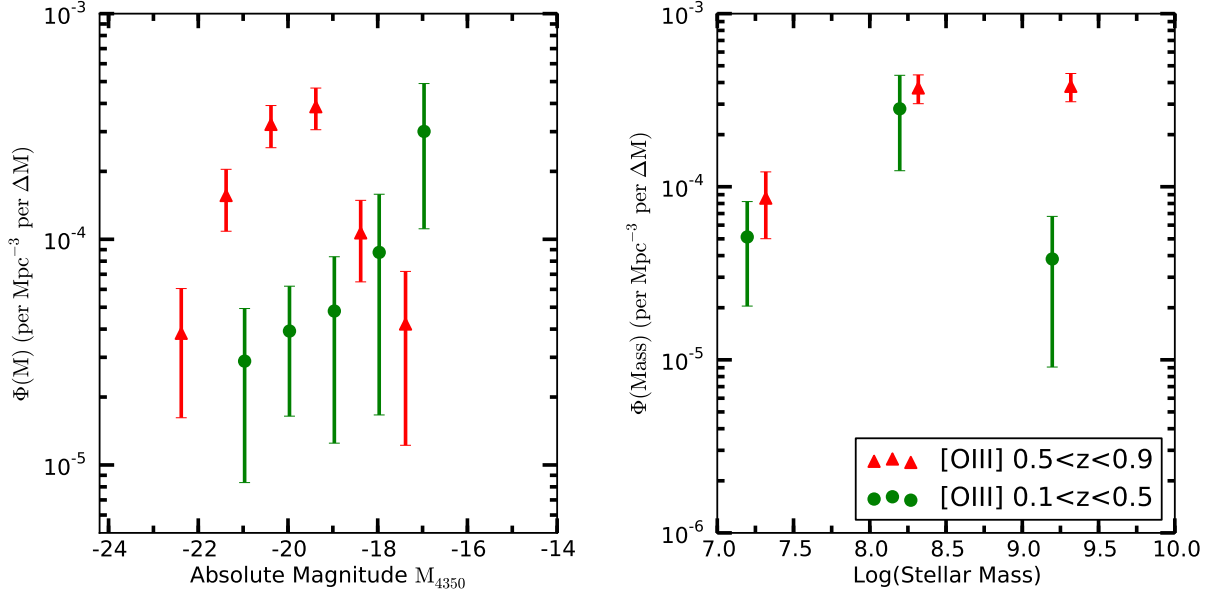


Fig. 20.— Left Panel: Luminosity functions of the 4350Å rest-frame absolute magnitude of the host GOODS galaxies where at least one [OIII] emission line region was detected with a corresponding SFR of  $1.7 \text{ M}_{\odot} \text{ yr}^{-1}$  or greater (corresponding to our flux limit at the maximum observable redshift of 0.9). We plot the densities of host galaxies in the lower redshift range of  $0.1 < z < 0.5$  using green circles, and the ones within the redshift range of  $0.5 < z < 0.9$  using red triangles. There is a strong decrease in the density of faint ( $M_{4350} > -19$ ) host galaxies at higher redshifts that does not exist at lower redshifts. Right Panel: The corresponding host galaxy mass function for the data shown on the left panel. There is a strong, ten-fold decrease in the number density of galaxies with [OIII] emission with stellar masses greater than  $10^9 \text{ M}_{\odot}$  in the lower redshift bin while the density of [OIII] emitting galaxies remain the same for less massive galaxies.

## REFERENCES

- Bertin, E., & Arnouts, S. 1996, A&AS, 117, 393
- Bruzual, G., Charlot, S., 2003, MNRAS, 344,1000
- Cardelli, J. A., Clayton, G. C., & Mathis, J. S. 1989, ApJ, 345, 245
- Cowie, L. L., Songaila, A., Hu, E. M., & Cohen, J. G. 1996, AJ, 112, 839
- Dahlen, T., Mobasher, B., Dickinson, M., et al. 2010, ApJ, 724, 425
- Dahlen, T. et al., in prep.
- Drozdosky, I., Yan, L., Chen, H.-W., et al. 2005, AJ, 130, 1324
- Efstathiou, G., Ellis, R. S., Peterson, B. A., 1988, MNRAS, 232
- Freedman, David; Diaconis, P. (1981). "On the histogram as a density estimator: L2 theory".  
Zeitschrift fr Wahrscheinlichkeitstheorie und verwandte Gebiete 57 (4): 453476.
- Fujita, S. S., Ajiki, M., Shioya, Y., et al. 2003, AJ, 125, 13
- Giavalisco, M., Ferguson, H. C., Koekemoer, A. M., et al. 2004, ApJ, 600, L93
- Grogin, N. A et al., in prep.
- Guo, Y., Giavalisco, M., Ferguson, H. C., Cassata, P., & Koekemoer, A. M. 2011, ApJ, 735,  
18
- Holwerda, B. W., Pirzkal, N., de Blok, W. J. G., et al. 2011, MNRAS, 416, 2437
- Hopkins, A. M., Connolly, A. J., Haarsma, D. B., & Cram, L. E. 2001, AJ, 122, 288
- Hopkins, A. M. 2004, ApJ, 615, 209
- Juneau, S., Dickinson, M., Alexander, D. M., & Salim, S. 2011, ApJ, 736, 104
- Kashikawa, N., Shimasaku, K., Malkan, M. A., et al. 2006, ApJ, 648, 7
- Kennicutt, R. C., Jr. 1998, ARA&A, 36, 189
- Koekemoer, A. M., Fruchter, A. S., Hook, R. N., & Hack, W. 2002, in Proc. 2002 HST  
Calibration Workshop, ed. S. Arribas, A. Koekemoer, & B. Whitmore (Baltimore:  
STScI), 33

- Kümmel, M., Walsh, J. R., Pirzkal, N., et al. 2009, *PASP*, 121, 59
- Laidler, V. G., Papovich, C., Grogin, N. A., et al. 2007, *PASP*, 119, 1325
- Lotz, J. M., Primack, J., & Madau, P. 2004, *AJ*, 128, 163
- Lotz, J. M., Jonsson, P., Cox, T. J., & Primack, J. R. 2008, *MNRAS*, 391, 1137
- Lotz, J. M., Jonsson, P., Cox, T. J., & Primack, J. R. 2010, *MNRAS*, 404, 590
- Ly, C., et al. 2007, *ApJ*, 657, 738
- Madau, P., Pozzetti, L., & Dickinson, M. 1998, *ApJ*, 498, 106
- Malkan, M., Teplitz, H., & McLean, I. 1995, *ApJ*, 448, L5
- Maraston C., Daddi, E., Renzini, A., Cimatti, A., Dickinson, M., Papovich, C., Pasquali, A., and Pirzkal, N. 2005, *MNRAS*, 362, 799
- Meurer, G. R. 1995, *Nature*, 375, 742
- Pirzkal, N., Pasquali, A., & Demleitner, M. 2001, *ST-ECF Newslett.*, 29, 5
- Noeske, K. G., Faber, S. M., Weiner, B. J., et al. 2007, *ApJ*, 660, L43
- Noeske, K. G., Faber, S. M., Weiner, B. J., et al. 2007, *ApJ*, 660, L47
- Peng, C. Y., Ho, L. C., Impey, C. D., & Rix, H.-W. 2002, *AJ*, 124, 266
- Pirzkal, N., Xu, C., Malhotra, S., et al. 2004, *ApJS*, 154, 501
- Pirzkal, N., Xu, C., Ferreras, I., et al. 2006, *ApJ*, 636, 582
- Pirzkal, N., Burgasser, A. J., Malhotra, S., et al. 2009, *ApJ*, 695, 1591
- Pirzkal, N., Rothberg, B., Nilsson, K. K., et al. 2012, *ApJ*, 748, 122
- Ravindranath, S., Giavalisco, M., Ferguson, H. C., et al. 2006, *ApJ*, 652, 963
- Rhoads, J. E., Malhotra, S., Dey, A., et al. 2001, *The New Era of Wide Field Astronomy*, 232, 196
- Sandage, A., Tammann, G. A., & Yahil, A. 1979, *ApJ*, 232, 352
- Schechter, P. 1976, *ApJ*, 203, 297
- Straughn, A. N., Meurer, G. R., Pirzkal, N., et al. 2008, *AJ*, 135, 1624



Straughn, A. N., Pirzkal, N., Meurer, G. R., et al. 2009, AJ, 138, 1022

Takahashi, M. I., Shioya, Y., Taniguchi, Y., et al. 2007, ApJS, 172, 456

Pre-print